

# Delineating the Roles of Mn, Al, and Co by Comparing Three Layered Oxide Cathodes with the Same Nickel Content of 70% for Lithium-ion Batteries

Michael Yi, Wangda Li, and Arumugam Manthiram\*

*McKetta Department of Chemical Engineering & Texas Materials Institute, The University of Texas at Austin, Austin, Texas, 78712, USA*

\*Corresponding author: [manth@austin.utexas.edu](mailto:manth@austin.utexas.edu)

## Abstract

High-nickel layered oxides continue to prevail in the energy storage market as the frontmost cathode candidates for next-generation lithium-ion batteries. Demand and development of  $\text{LiNi}_{1-x-y}\text{Mn}_x\text{Co}_y\text{O}_2$  (NMC) and  $\text{LiNi}_{1-x-y}\text{Co}_x\text{Al}_y\text{O}_2$  (NCA) cathodes are rampantly increasing, particularly for the electric vehicle (EV) industry. However, the continued presence of cobalt in NMC and NCA cathodes raise global concerns due to geopolitical and ethical issues attributed with Co sourcing. We herein introduce a novel cobalt-free, high-nickel cathode  $\text{LiNi}_{0.7}\text{Mn}_{0.25}\text{Al}_{0.05}\text{O}_2$  (NMA70) and benchmark it against Co-containing  $\text{LiNi}_{0.7}\text{Mn}_{0.15}\text{Co}_{0.15}\text{O}_2$  (NMC70) as well as Co- and Al-free  $\text{LiNi}_{0.7}\text{Mn}_{0.3}\text{O}_2$  (NM70) cathodes with equivalent 70% Ni contents that are all synthesized in-house. NMA70 displays a high initial C/10 capacity of  $210 \text{ mA h g}^{-1}$ , matching that of NMC70 in half cells with a cutoff voltage of 4.5 V. NMA70 also exhibits impressive high-voltage full cell cycling performance with a cutoff voltage of 4.4 V with a nearly identical capacity retention of 83% compared to 82% for NMC70 after 300 cycles. Postmortem X-ray photoelectron spectroscopy (XPS), high-angle annular dark-field scanning transmission electron microscopy (HAADF-STEM), and electron energy loss spectroscopy (EELS) analyses indicate a thinner cathode-electrolyte interface (CEI) developed in NMA70 compared to that in NM70 and unveil a more robust solid-electrolyte interface (SEI) passivation on the graphite anode amongst all samples. The benefits of Al doping are additionally highlighted with enhanced high-voltage CEI and thermal stabilities in NMA70. This

work assesses the roles of Mn, Al, and Co to demonstrate both the practicality and feasibility of synthesizing cobalt-free, high-nickel cathodes that are promising alternatives to current NMC- and NCA-based cathodes.

## Introduction

The adoption of layered-oxide cathodes in lithium-ion batteries (LIBs) has led to unprecedented development in portable electronic devices and electric vehicles (EVs) due to their high energy and power densities.<sup>1-3</sup> This began with the introduction of the layered-oxide cathode LiCoO<sub>2</sub> (LCO) developed by Goodenough's group in 1980, which brought new insights and promise towards LIBs.<sup>4</sup> However, factors, such as the limited upper cutoff voltage of ~ 4.3 V vs. Li/Li<sup>+</sup> for LCO along with the toxicity and hefty cost of cobalt for large applications, have caused a shift from LCO to Ni-layered oxides, such as LiNi<sub>1-x-y</sub>Mn<sub>x</sub>Co<sub>y</sub>O<sub>2</sub> (NMC) and LiNi<sub>1-x-y</sub>Co<sub>x</sub>Al<sub>y</sub>O<sub>2</sub> (NCA), due to their lower cost and similar or higher energy densities, which help to bolster EV production.<sup>5-7</sup> For EVs to compete with modern internal combustion engine vehicles, the US Department of Energy estimates that the LIBs powering them will need to reach a specific energy of 350 W h kg<sup>-1</sup> at the cell level.<sup>2,8</sup> LIBs are unlikely to achieve this specific capacity if the cathode Ni content is too low, which is leading to the push for higher Ni cathodes, such as NMC and NCA with ≥ 80 mol % Ni.

However, many inherent problems are associated with high-Ni cathodes. Difficulties in keeping all the Ni as Ni<sup>3+</sup> during synthesis leads to lithium deficiency and lithium-nickel mixing where the Ni<sup>2+</sup> ions migrate into the Li<sup>+</sup> layers of the oxide structure because of their similar ionic radii. The cation mixing impedes Li<sup>+</sup> diffusion, which can worsen during cycling and lead to insulating NiO rock-salt phase formation on the cathode surface, compromising the battery cycle life.<sup>9-12</sup> Additionally, highly reactive Ni<sup>4+</sup> ions are generated at high states of charge, which

accelerates electrolyte decomposition and thicken the cathode surface with the resulting decomposition products.<sup>10,13</sup> High-Ni cathodes are also susceptible to particle cracking and ensuing active material loss due to large anisotropic lattice and volume changes during cycling.<sup>9,14</sup> This is why Co is still heavily used in the current high-Ni NMC and NCA compositions as it is known to help suppress Li/Ni mixing, improve rate capability, and reduce the overall total Ni concentration to mitigate surface reactivity and particle cracking.<sup>15-18</sup> The main problem, therefore, circles back to Co usage since the demands for the Co-containing, high-Ni cathodes are exponentially increasing. In addition to the toxic and scarce nature of Co, it is mainly sourced by mining from the Democratic Republic of the Congo, a country afflicted with geopolitical instability and child labor ethics violations.<sup>19,20</sup> These issues have led to erratic cobalt prices over the past few years which could worsen as demands for higher energy density batteries increase.<sup>21,22</sup> With growing concerns with cobalt sourcing and regulations, it is imperative to pursue high-Ni cathodes for LIBs that have lower Co contents, ideally being completely void of it. The current dilemma, therefore, is finding substitutes for replacing cobalt while maintaining the high energy density and cycle life requirements set by industry.

Among a variety of dopants available, Mn and Al are mainly utilized in current high-nickel cathodes, as seen with the incorporation of both elements in NMC and NCA cathodes. Mn has been widely studied as the most common dopant aside from Co for its role in cycling stability but also its noticeable improvement in thermal stability, which is a crucial parameter to consider for EV batteries.<sup>23,24</sup> Unlike most dopants, Mn can be incorporated in Ni-layered oxide cathodes up to 50 mol % without any structural changes into other phases. While Mn doping is shown to stabilize cycling performance and phase transitions at high voltages, a large amount compromises the capacity as well as increased Li/Ni mixing due to the formation of more Ni<sup>2+</sup> ions to charge balance

the  $\text{Mn}^{4+}$  ions in the layered structure.<sup>25</sup> Mn-rich cathodes are also susceptible to transition-metal dissolution, a phenomena extensively seen with Mn-based spinel cathodes.<sup>26</sup> Al, in contrast, is known for stabilizing the transition-metal layer with its increased metal-oxygen bond strength, thereby reducing transition-metal dissolution and Li/Ni mixing. However, Al incorporation is limited to 5-6 mol % as any excess amounts can lead to Al-based impurities and external phases.<sup>27,28</sup>

Therefore, an investigation combining both dopants into Ni-rich cathodes without Co is warranted and was demonstrated recently in our group by introducing a new Co-free cathode class:  $\text{LiNi}_{1-x-y}\text{Mn}_x\text{Al}_y\text{O}_2$  (NMA) with the composition of  $\text{LiNi}_{0.90}\text{Mn}_{0.05}\text{Al}_{0.05}\text{O}_2$ .<sup>29,30</sup> This cathode showed superior full cell cycling performance compared to its Co-containing baselines  $\text{LiNi}_{0.90}\text{Mn}_{0.05}\text{Co}_{0.05}\text{O}_2$  and  $\text{LiNi}_{0.90}\text{Co}_{0.05}\text{Al}_{0.05}\text{O}_2$ .

The success of this work suggests further opportunities in exploring the compositional design space of the NMA class, particularly regarding how a lowering of Ni content will affect performance, since the tradeoffs of removing Co become more critical at lower Ni contents particularly due to the decreased capacity and poor rate capability due to cation mixing. This work herein introduces an alternative NMA composition:  $\text{LiNi}_{0.7}\text{Mn}_{0.25}\text{Al}_{0.05}\text{O}_2$  (NMA70) in order to benchmark how it performs relative to its NMC counterpart in  $\text{LiNi}_{0.7}\text{Mn}_{0.15}\text{Co}_{0.15}\text{O}_2$  (NMC70) and Co- and Al-free  $\text{LiNi}_{0.7}\text{Mn}_{0.3}\text{O}_2$  (NM70) and to characterize how Mn, Al, and Co doping affects cathode performance. A diverse set of characterization techniques, such as focused ion beam scanning electron microscopy (FIB-SEM), energy dispersive X-ray spectroscopy (EDX), *ex-situ* X-ray diffraction (XRD), electrochemical impedance spectroscopy (EIS), X-ray photoelectron spectroscopy (XPS), transmission electron microscopy (TEM), and differential scanning calorimetry (DSC) along with high-voltage electrochemical testing are employed to methodically

examine each cathode. It is shown that the addition of Al helps reduce Li/Ni mixing and further improves the electrochemical and thermal stabilities of the cathode. The enhancements are attributed to the mitigated electrode-electrolyte interfacial reactions of NMA70 brought upon with Al, indicating its suitability as a counterbalancing dopant in place of Co. Overall, the results highlight the potential viability of NMA70 as a Co-free alternative cathode.

## Experimental Section

**Materials.** The  $\text{LiNi}_{0.7}\text{Mn}_{0.25}\text{Al}_{0.05}\text{O}_2$  (NMA70),  $\text{LiNi}_{0.7}\text{Mn}_{0.15}\text{Co}_{0.15}\text{O}_2$  (NMC70), and  $\text{LiNi}_{0.7}\text{Mn}_{0.3}\text{O}_2$  (NM70) samples were synthesized in-house via metal hydroxide coprecipitation and calcination. For the coprecipitation, 2.0 M aqueous solutions of  $\text{NiSO}_4 \cdot 6\text{H}_2\text{O}$ ,  $\text{CoSO}_4 \cdot 7\text{H}_2\text{O}$ ,  $\text{MnSO}_4 \cdot \text{H}_2\text{O}$ , and  $\text{Al}(\text{NO}_3)_3 \cdot 9\text{H}_2\text{O}$  were first prepared with the appropriate molar ratios of each metal ( $\text{Ni} : \text{Mn} : \text{Al} = 0.7 : 0.25 : 0.05$ ,  $\text{Ni} : \text{Mn} : \text{Co} = 0.7 : 0.15 : 0.15$ , and  $\text{Ni} : \text{Mn} = 0.7 : 0.3$ ). These solutions were then pumped into a 10 L batch stirred tank reactor filled with an aqueous solution of KOH and  $\text{NH}_4\text{OH}$  all under an inert argon (Ar) atmosphere (due to the oxidative instability of  $\text{Mn}(\text{OH})_2$ ).<sup>31</sup> Separate concentrated aqueous solutions containing 4.0 M KOH and 14.8 M  $\text{NH}_4\text{OH}$  were also simultaneously pumped into the tank reactor to maintain a constant pH ( $\sim 11.3$ ) for each synthesis. The temperature ( $\sim 50$  °C) and stirring speed ( $\sim 600$  rpm) of the tank reactor were all carefully controlled during the coprecipitation synthesis. The synthesized  $\text{Ni}_{0.7}\text{Mn}_{0.25}\text{Al}_{0.05}(\text{OH})_2$ ,  $\text{Ni}_{0.7}\text{Mn}_{0.15}\text{Co}_{0.15}(\text{OH})_2$ , and  $\text{Ni}_{0.7}\text{Mn}_{0.3}(\text{OH})_2$  precursors were then washed with deionized water, filtered, and dried at 100 °C overnight. To finally obtain the NMA70, NMC70, and NM70 samples, their respective metal hydroxide precursors were homogeneously mixed with  $\text{LiOH} \cdot \text{H}_2\text{O}$  (molar ratios of  $\text{Li} : (\text{Ni} + \text{Mn} + \text{Al or Co}) = 1.01 : 1$  and  $\text{Li} : (\text{Ni} + \text{Mn}) = 1.05 : 1$ ) and calcined at 820 °C (for NMA70 and NMC70) or 830 °C (for NM70) for 15 h under oxygen atmosphere.

**Electrochemical Testing.** Cathode slurries were prepared by mixing the active materials, conductive carbon (Super P), and poly(vinylidene fluoride) (PVDF) binder in a 90 : 5 : 5 weight ratio along with N-methyl-2-pyrrolidone (NMP). The slurries were then casted onto an Al foil with active material loadings of  $\sim 10 \text{ mg cm}^{-2}$  and were subsequently roll-pressed and dried in a vacuum oven overnight at  $120 \text{ }^\circ\text{C}$ . Electrodes were made from the dried casts with a 1.2 cm round punch. CR2032 half cells were then fabricated by pairing these cathodes with Li-metal chips as the anodes and Celgard 2500 separator. LP57 electrolyte consisting of 1.0 M  $\text{LiPF}_6$  in ethylene carbonate (EC) and ethyl methyl carbonate (EMC) (3 : 7 wt. ratio) along with 2 wt. % of vinylene carbonate (VC) was used in the cells. The cells were cycled between 2.8 and 4.5 V versus  $\text{Li}^+/\text{Li}$  with a C/10 rate for three formation cycles followed by C/3 rate cycling at  $25 \text{ }^\circ\text{C}$  ( $1\text{C} = 180 \text{ mA g}^{-1}$ ). Similarly, cathode electrodes were cast with areal loadings of  $\sim 1.7 \text{ mA h cm}^{-2}$  and were paired with MCMB graphite anodes for fabricating full cells with an N/P ratio of  $\sim 1.1$ . The full cells were cycled between 2.5 and 4.4 V with three C/10 rate formation cycles and then were cycled with C/2 charge – 1C discharge rates. The cells were also cycled at a C/3 rate every 100 cycles for capacity checks. All galvanostatic charge and discharge steps were coupled with constant voltage steps (CCCV). The cells were all tested on Arbin battery cyclers. Electrochemical impedance spectroscopy (EIS) measurements were performed on the full cells (charged to 3.7 V prior to EIS measurements) with an impedance spectrometer (Solartron 1260A) by applying a 5 mV potential perturbation in the frequency range of 1 MHz to 1 mHz.

**Materials Characterization.** The morphologies of the cathode precursors and calcined particles were examined with a FEI Quanta 650 field emission scanning electron microscope (SEM). Cross-sectional focused ion beam (FIB) milling along with the respective SEM and energy dispersive X-ray spectroscopy (EDX) imaging were carried out on the fresh cathode samples with

a Scios 2 HiVac DualBeam FIB/SEM system. Powder X-ray diffraction (XRD) measurements were conducted on a Rigaku Miniflex 600 X-ray diffractometer with Cu K $\alpha$  radiation ( $\lambda = 1.54184$  Å) in the  $2\theta$  range of  $10.0^\circ - 80.0^\circ$  with a scan step of  $0.02^\circ$  and a scan rate of  $0.583^\circ \text{ min}^{-1}$ . Rietveld refinements of the XRD patterns were conducted with the GSAS-II software package.<sup>32</sup> Chemical compositions of the cathode materials were analyzed with inductively coupled plasma optical emission spectroscopy (ICP-OES) (Varian 715 ES). X-ray photoelectron spectroscopy (XPS) analysis of the cycled full cell electrodes was carried out on an Axis Ultra DLD spectrometer (Kratos) with an Al K $\alpha$  radiation source (1486.6 eV). Transmission electron microscopy (TEM) analyses were performed using a JEOL NEOARM equipped with a probe corrector for scanning transmission electron microscopy (STEM). An accelerating voltage of 80 kV was used to minimize damage. For both XPS and TEM preparation, the cycled electrode samples were rinsed with dimethyl carbonate (DMC), dried in an argon-filled glovebox, and then transferred to the analyzer via an air-free capsule. Thermal stabilities of the cathode samples were assessed through differential scanning calorimetry (DSC) experiments with a NETZSCH STA 449 Jupiter thermal analysis system. For DSC, the cathode samples were each charged to 80% of their maximum theoretical specific charge capacities ( $\sim 220 \text{ mA h g}^{-1}$ ) following two C/10 formation cycles in Li-metal half cells. The charged cathodes were harvested from the disassembled cells and rinsed in dimethyl carbonate (DMC) in an Ar-filled glovebox. The cathodes were then dried and collected into a tightened ( $\sim 0.5 \text{ N m}$ ) stainless steel crucible along with added electrolyte in a  $\sim 6 : 4$  cathode : electrolyte weight ratio. The DSC tests were conducted with a  $10^\circ \text{ C min}^{-1}$  heating rate from  $30^\circ \text{ C}$  to  $350^\circ \text{ C}$  under flowing Ar gas.

## Results and Discussion

**Morphological, Elemental, and Structural Characterization.** Following coprecipitation and calcination, the synthesized samples were observed under SEM as shown in Figure 1a – c and in Figures S1 and S2. All samples displayed a homogeneous and spherical morphology with similar particle sizes of ~ 13 – 16  $\mu\text{m}$  in diameter. Note that the variations in the primary particle size and morphologies seen in Figure S2 are due to compositional differences in each cathode. The elemental distributions in each sample were confirmed through cross-sectional SEM and EDS imaging in Figure 1d. All three samples exhibited uniform elemental distributions throughout the bulk to the surface of the particles. The homogeneity of Al indicated the successful coprecipitation of the NMA70 precursor. This is especially important as Al doping is notoriously difficult due to the ease at which  $\text{Al}(\text{OH})_3$  can precipitate first compared to the other metal ions in solution during coprecipitation. This could lead to nonuniform Al phase segregation that can form after calcination.<sup>33,34</sup> Al can also cause noticeable changes in primary particle morphology following calcination, as is seen with the different primary particle sizes of NMA70 compared to the other cathodes in Figure S2.<sup>29</sup> ICP results in Figure 1e also indicate that the elemental molar compositions present in the samples nearly match the targeted values of the NMA70, NMC70, and NM70 cathodes.

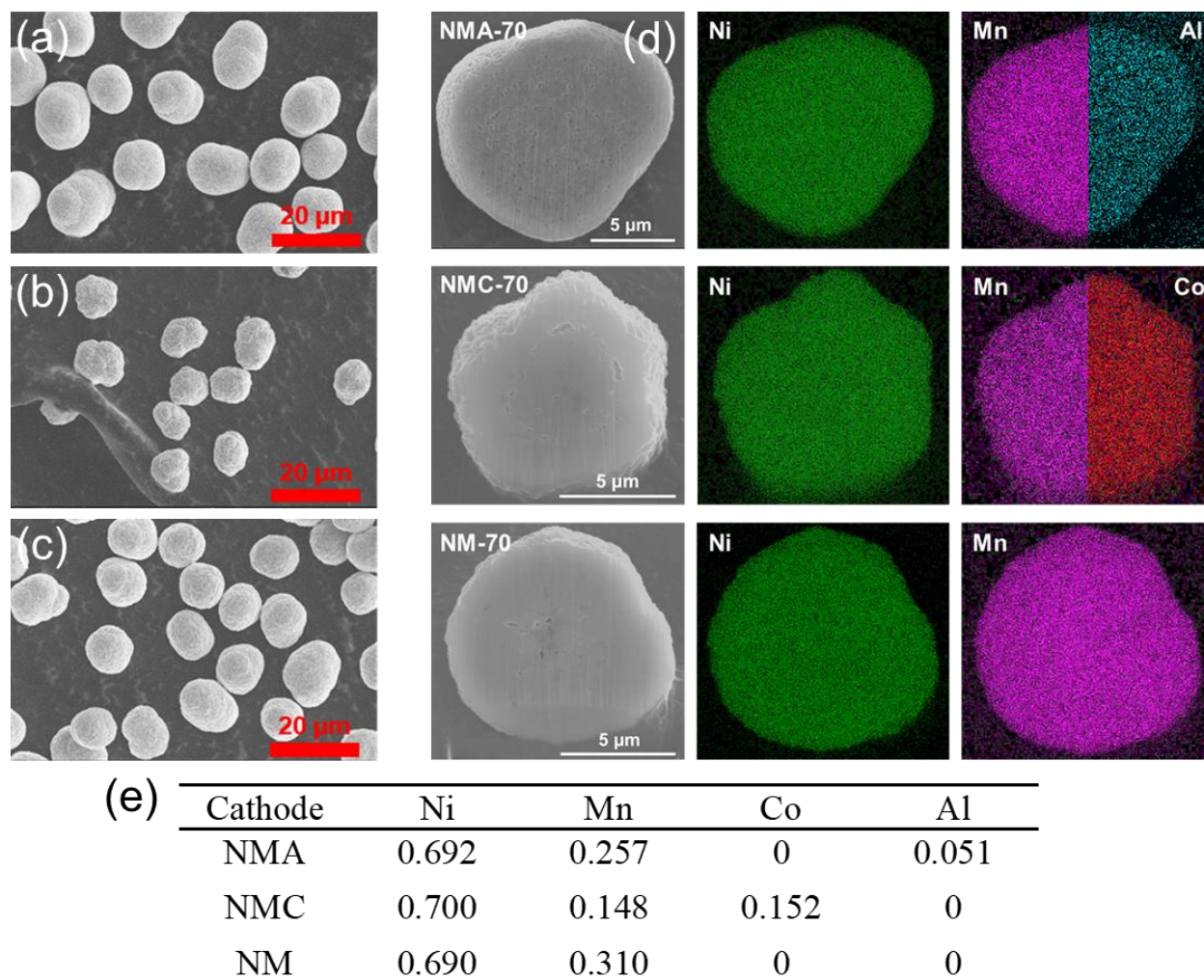


**Figure 1.** SEM images of calcined (a) NMA70, (b) NMC70, and (c) NM70 samples. (d) FIB cross-sectional SEM/EDS mappings showing the elemental distribution for each sample after calcination. (e) ICP-OES data of the samples after calcination.

XRD characterizations along with the Rietveld refinements of the patterns are given for each sample as shown in Figure 2 and Table 1 (see Tables S1-S3 for additional tabulated refinement data). All three patterns display peaks indicative of the hexagonal  $\alpha$ - $\text{NaFeO}_2$  structure with the  $R\bar{3}m$  space group, with no other impurity peaks. Rietveld refinement results of NMA70 are shown in Figure 2a, with an  $I(003)/I(104)$  ratio of 1.05, in which a larger ratio indicates less cation disorder, along with a tabulated Li/Ni mixing value of 6.4%. NMC70 refinement results in Figure

2b present reduced Li/Ni cation disorder with a larger  $I(003)/I(104)$  ratio of 1.16 and 3.8% mixing. The refinement results of NM70 in Figure 2c display the largest degree of Li/Ni mixing among the three cathodes with a noticeably lowered  $I(003)/I(104)$  ratio of 0.94 and a 9.3% cation disorder. Note that the intensities used to calculate the  $I(003)/I(104)$  ratios are determined through the integrated peak area intensities based on the XRD patterns. It is logical to have such high  $\text{Ni}^{2+}$  mixing in the Li layers with NM70 as 30% of the entire transition metal (TM) composition is  $\text{Mn}^{4+}$ , which will certainly induce a significant amount of  $\text{Ni}^{2+}$  formation for the sake of charge balancing in the TM layer.<sup>25</sup>

The advantageous role of  $\text{Al}^{3+}$  in the NMA70 cathode with only a 5% molar incorporation can be seen through the reduction in the Li/Ni mixing percentage compared to that of NM70. Previous studies have shown that the strong Al-O bonding energy ( $512.0 \text{ kJ mol}^{-1}$  for Al-O versus  $382.0 \text{ kJ mol}^{-1}$  for Ni-O) strengthens the TM-O layers by decreasing the Ni-O bond length and prevents formed  $\text{Ni}^{2+}$  from migrating to the Li layer, both reducing the Li/Ni mixing and allowing for more  $\text{Li}^+$  utilization and thus higher capacity and stability.<sup>28,35-37</sup> The reduced unit cell volumes of NMA70 and NMC70 compared to NM70 corroborate their lowered Li/Ni mixing percentages, as this implies that the TM layer maintains more  $\text{Ni}^{3+}$ . With  $\text{Ni}^{3+}$  having a smaller ionic radius of  $0.56 \text{ \AA}$  compared to  $\text{Ni}^{2+}$  with  $0.69 \text{ \AA}$ , a larger presence of  $\text{Ni}^{3+}$  will therefore induce contractions of the overall unit cell lattice parameters and volumes.<sup>38</sup> NMC70 unsurprisingly has the lowest amount of mixing and the smallest lattice parameter dimensions due to the significant presence of  $\text{Co}^{3+}$  that replaces essentially half of the  $\text{Mn}^{4+}$  compared to both NM70 and NMA70, hence maintaining a larger proportion of  $\text{Ni}^{3+}$  to  $\text{Ni}^{2+}$ .

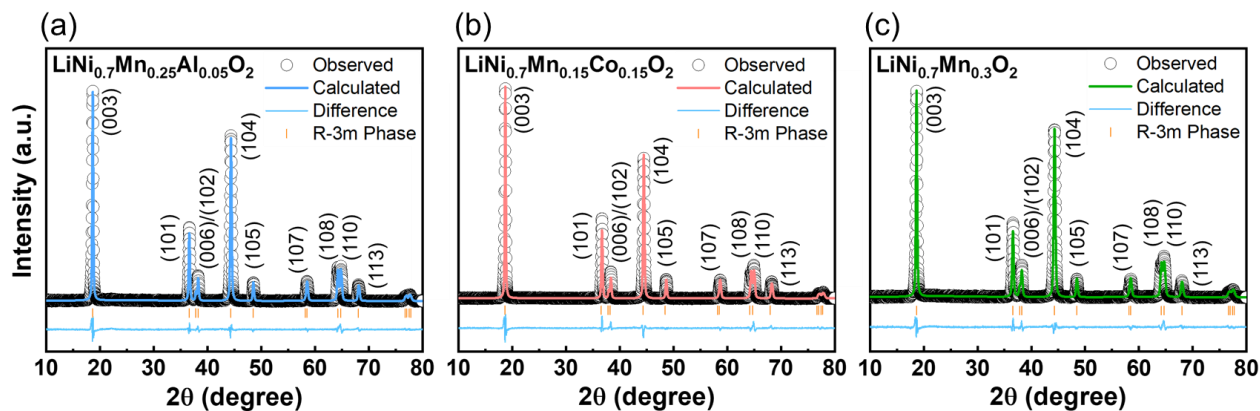


**Figure 2.** Rietveld refinement results of the XRD patterns of pristine (a) NMA70, (b) NMC70, and (c) NM70.

**Table 1.** Crystallographic parameters of NMA70, NMC70, and NM70 obtained with Rietveld refinement of the XRD patterns

Sample	c (Å)	a (Å)	Unit cell volume (Å <sup>3</sup> )	$I(003)/I(104)$	Li <sup>+</sup> /Ni <sup>2+</sup> mixing (%)
NMA70	14.252	2.875	102.032	1.05	6.4
NMC70	14.217	2.870	101.423	1.16	3.8
NM70	14.259	2.879	102.337	0.94	9.3

**Electrochemical Performance.** The electrochemical performances of the cathodes are displayed in Figure 3. The effects of Al<sup>3+</sup> incorporation on the charge-discharge curves are shown in Figure 3a. Compared to NM70, which has a discharge capacity of 185 mA h g<sup>-1</sup>, NMA70 has a remarkable increase in capacity to 210 mA h g<sup>-1</sup>, on par with that of NMC70. NM70 shows an increased voltage shoulder during charging capping at around 3.7 V compared to 3.6 V seen with NMA70 and NMC70. This is alternatively shown in the dQ dV<sup>-1</sup> curves in Figure 3b, which illustrate NMA70 and NMC70 both having earlier peak onset voltages of around 3.6 V compared with 3.7 V for NM70 during charge. This peak, formed around the voltage range of ~ 3.5 to 3.8 V, is commonly attributed to the H1 to M phase transformation in Ni-rich cathodes.<sup>39</sup> Furthermore, a higher voltage at which this peak occurs could be indicative of more polarization and kinetic hindrances present in the cathode due to slower Li<sup>+</sup> diffusion stemming from large migration

energy barriers during the charge onset.<sup>17,40,41</sup> During discharge, however, both NM70 and NMA70 show a peak at ~ 4.3 V that is shifted higher than that in NMC70 (~ 4.2 V). Peaks around this range are indicative of H2 to H3 phase transformation.<sup>39,40</sup> The higher peak shifts of NM70 and NMA70 initially might suggest better kinetics than NMC70, but this cannot be the case for NM70 as the rate capability data in Figure 3c shows this is not true. Therefore, this indicates that the initial peak potential shifts seen here can stem from the intrinsic redox activity that is dependent on and unique to the material composition and structure. This may also indicate that the peak position during charge is, at least in part, intrinsic to the material.

However, this phenomenon around 3.5 to 3.8 V is shown to worsen with a higher degree of Li/Ni mixing due to Ni<sup>2+</sup> ions occupying the available sites for Li<sup>+</sup> intercalation.<sup>39,41</sup> Therefore, the delay in the H1 to M peak occurrence for NM70 at around 3.7 V could translate to less Li<sup>+</sup> extraction during charge, resulting in less Li<sup>+</sup> insertion during discharge at the same operating voltage ranges as for NMA70 and NMC70 due to its poor kinetics stemming from higher cation disorder which worsens over continual cycling. This is seen in Figure 3a, which clearly shows the reduced discharge capacity at the end of discharge for NM70 and can potentially explain its unexpectedly low capacity compared to NMA70, since Al is widely known to suppress cation mixing and improve Li<sup>+</sup> kinetics due its structural stabilization of the TM lattice.<sup>42,43</sup> The worsening degradation is also seen in Figures S3 and S4 which show, respectively, the evolutions of voltage curves and dQ dV<sup>-1</sup> curves for each cathode. NMA70 and NMC70 display greatly reduced overpotential growth during the onsets of charge and discharge and suppressed polarization increase compared to that of NM70 which portrays clear signs of structural and kinetic degradation. Moreover, the large initial voltage drops during the discharge of NM70 in both half and full cells shown in Figure 3a and 3f indicate that the surface impedance is one of the dominant

contributors to the capacity fade and will be discussed in further detail in the following sections. The peak shifts in the NM70  $dQ/dV^{-1}$  plot can, therefore, additionally be attributed to the SEI impedance moving the overall curve downward, independent of the extent of lithiation in the cathode and possible phase transitions. It is still surprising to see such a large capacity increase with NMA70, but the effects of Al notably improving capacity, particularly in lower Ni, Co-free materials, have in fact been reported before.<sup>35-37,44</sup> Determining the mechanistic insights behind the capacity increase due to Al incorporation warrants a future investigation, but is not the main focus of this study.

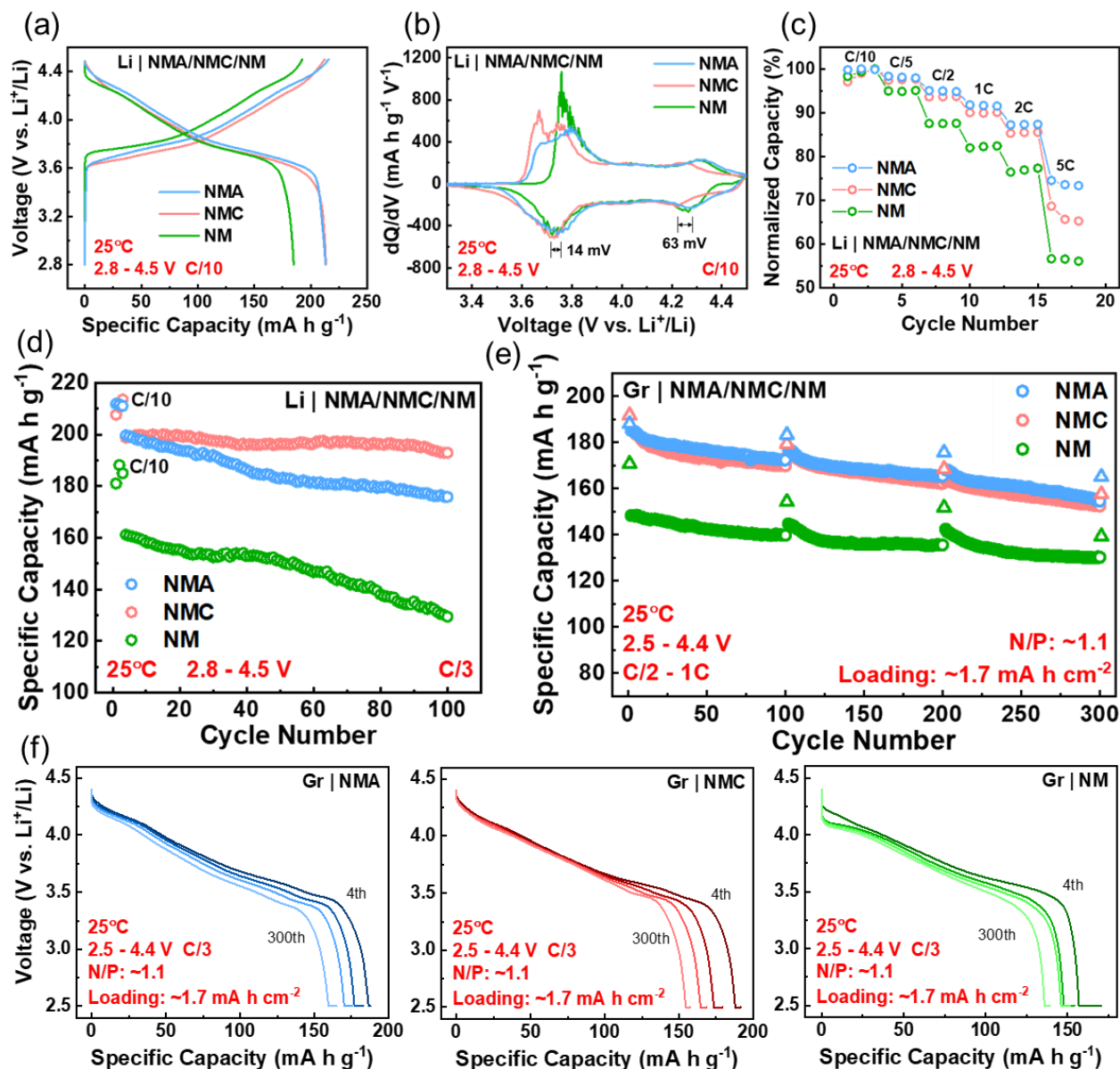
Additionally, the  $dQ/dV^{-1}$  curves indicate that the phase transition peaks during discharge for NMA70 around 3.7 and 4.3 V occur, respectively, 14 mV and 63 mV higher than those of NMC70. This implies NMA70 has a higher average discharge voltage than NMC70, which is beneficial as it leads to an increased energy density.<sup>29</sup> NMC70 and NM70 also both exhibit sharp peaks of the H1 to H2 phase transition between 3.6 and 3.8 V while NMA70 shows more of a single broad peak, indicative of a smoother phase transition throughout this range.<sup>39,45</sup> Figure 3c illustrates the superior rate capability of NMA70 compared to that of NM70, but comparable to that of NMC70, across the various rates tested, further indicating the kinetic improvements brought by Al incorporation. It is worth noting that slightly larger capacity drops from C/5 to C/2 and from 2C to 5C are visible, which could be attributed to increased IR drops from higher current rates and not just kinetic limitations. The large capacity drops, especially at 5C, could also be due to other concentration-dependent physical phenomena; however, the overall results still show the benefits brought by Al incorporation into NMA70 compared with NM70.

Figure 3d presents the cycling performance of the cathodes in half cells. The capacity retentions of NMA70, NMC70, and NM70 are, respectively, 88%, 97%, and 80% after 100 cycles

at a C/3 rate. The excellent retention of NMC70 was expected as it has been shown to be a stable cathode material.<sup>46,47</sup> The more notable feature, however, is the large capacity increase in NMA70 compared to NM70, with the former having an initial C/3 discharge capacity of 202 mA h g<sup>-1</sup> similar to that of NMC70 while the latter having 162 mA h g<sup>-1</sup>. Additionally, NMA70 exhibits improved capacity retention, which is complimented by its increased coulombic efficiency (CE) near the end of cycling compared to the two baselines shown in Figure S5.

Long-term full cell cycling of the cathodes paired with graphite anodes is displayed in Figure 3e. By cycling to a high-voltage cutoff of 4.4 V in full cells ( $\sim 4.5 V_{Li}$ ), it was anticipated that the cells will show high initial capacities in order to compete in energy density with ultrahigh Ni cathodes ( $\geq 90\%$  Ni) cycled at slightly lower voltages, albeit with moderate cyclability degradation. After 300 cycles at a C/2 charge – 1C discharge rate, NMA70 interestingly shows nearly identical discharge capacities and cycling performance to that of NMC70 with retentions of, respectively, 83% and 82%, clearly deviating from the performances seen in Li-metal half cells. This deviation can be attributed to differences in transition-metal dissolution experienced by the cathodes, which compromises the passivation of the electrode-electrolyte interfaces that develop over long-term cycling in full cells and will be further discussed later. In half cells, this phenomenon may be overshadowed by the unlimited Li supply from Li-metal anode and with only 100 cycles compared to the long-term cycling of full cells paired with graphite anode.<sup>29</sup> Additionally, it is shown that transition-metal dissolution and resulting chemical crossover have little effect on the Li-metal anode in half cells due to the following: transition-metal dissolution has less effect on an inherently reactive Li metal anode, the crossover products are diluted in a thicker SEI, and form in lower quantities due to the limited cyclability for Li-metal half cells.<sup>48</sup> NM70 also contrarily shows a slightly higher full cell capacity retention of 88% compared to the

other samples. However, NM70 also displays a large initial capacity penalty of  $37 \text{ mA h g}^{-1}$ , lower than the values of NMA70 and NMC70.



**Figure 3.** Electrochemical performance and characterization of NMA70, NMC70, and NM70 in half cells (vs. Li-metal) and in full cells (vs. graphite) at 25°C. (a) Charge-discharge voltage profiles of the 3<sup>rd</sup> formation cycle, (b)  $dQ/dV$  curves of the 3<sup>rd</sup> formation cycle, and (c) normalized rate capability tests. (d) Cycling performance in half cells. (e) Full cell cycling performance at C/2 charge – 1C charge rates (circular points) of NMA70, NMC70, and NM70 starting at the 4<sup>th</sup> cycle after three C/10 formation cycles, including the capacity check at every 100<sup>th</sup> cycle at C/3 rates (triangular points). (f) Discharge voltage profiles of the C/3 capacity checks at every 100 cycles of NMA70, NMC70, and NM70.

To better understand the capacity fading phenomena of each cathode, C/3 slow discharge capacity checks were performed every 100 cycles for each sample and are shown in Figure 3e. (See Figure S6 for the sole C/3 capacity check plot). Similar initial capacity trends are seen as in the regular operation cycles, with NMA70 and NMC70 being close in values and with NM70 having a noticeably lower capacity. However, it becomes clear near the end of cycling that NMA70 yields better capacity retention among the three samples. When normalized by the first C/3 discharge capacity, the retentions of NMA70, NMC70, and NM70 after the 300<sup>th</sup> cycle are, respectively, 88%, 82%, and 81%. NMA70 now shows the greatest capacity retention while NM70 shows the lowest, opposite to what is seen with the regular long-term cycling retention. This indicates that NMA70 has better cyclability compared the other two cathodes with slower current cycling rates and reduced polarization, but also suggests that NMA70 has a slightly lower rate capability compared to NMC70 after 300 cycles given the marginal increase in capacity drop from C/3 to 1C. On the other hand, NM70 displays the largest drops from its C/3 to 1C discharge capacities compared to those of NMC70 and NMA70, which further highlight the poor rate capability and large polarization experienced by this sample at 1C discharge rates.

The C/3 discharge voltage-capacity curves are also plotted in Figure 3f. NMA70 and NMC70 curves show a steady capacity fade over each 100<sup>th</sup> cycle with slight polarization increase in the beginning of each discharge. NM70, on the other hand, fades comparable to the other two cathodes from 4<sup>th</sup> to 100<sup>th</sup> cycle, shows slight capacity drops between 100<sup>th</sup> and 200<sup>th</sup> cycle, and then abruptly declines in capacity after 300<sup>th</sup> cycle. Following the capacity check of the 4<sup>th</sup> formation cycle, large voltage drops are displayed during the onset of discharge for each successive voltage curve of NM70, indicative of severe polarization increase and large impedance buildup throughout

cycling, more so than that with NMA70 and NMC70. The specific reasons for the relatively lower capacity decrease between 100<sup>th</sup> and 200<sup>th</sup> cycles of NM70 are not entirely clear. The lower capacity of NM70 compared to NMA70 or NMC70 indicates that it utilizes less lithium at the same potentials due to its poor kinetics. It is possible then that NM70 experiences less structural deterioration as it does not experience the full range of lithium extraction and insertion at the same states of charge compared to both NMA70 and NMC70 while cycling and can perhaps result in relatively lesser capacity fade. However, the significantly lowered initial capacity, increased voltage polarization, larger capacity fade near the end of cycling, and the worst capacity retention at a slower rate of C/3 following the 300<sup>th</sup> cycle highlight that the disadvantages of NM70 are much more significant than the marginally better 1C discharge capacity retention among the three cathode samples.

Overall, the enhanced cyclability of NMA70 is attributed to the benefits of increased capacity, improved kinetics, and reduced polarization brought by Al incorporation compared to NM70. The similarities seen in the capacity, retention, and voltage profiles between NMA70 and NMC70 throughout cycling also highlight the meaningful impact that a mere 5% Al doping has versus 15% Co and suggests that NMA70 can be deemed more favorably comparable to NMC70 as a potential cobalt-free alternative.

**Electrode/Electrolyte Interface Analysis.** The impedance growth of each full cell was determined with EIS after the 4<sup>th</sup>, 100<sup>th</sup>, 200<sup>th</sup>, and 300<sup>th</sup> cycles and is shown in Figure S7a. By applying a small voltage perturbation across a wide frequency range, the complex impedances evolving in the cells during cycling can be decoupled into specific contributions to resistance to better understand the cell capacity fading phenomena.<sup>49,50</sup> The individual resistance contributions are determined by fitting the EIS data with an equivalent circuit model shown in Figure S7b. The

impedance spectra consist of two main resistance components determined by two semicircles. The first semicircle in the high-medium frequency regime is typically ascribed to surface-film resistance stemming from the growth of the electrode-electrolyte interfaces.<sup>51–53</sup> Recent studies, however, show this understanding is oversimplified as it does not consider other important attributes to impedance such as the intrinsic properties of electrode materials as well as the contact between electrodes and the current collectors. It has in fact been shown that the main contribution to the first semicircle resistance is not so much due to a surface film, but rather to the poor conductive contact between the cathode active material and the current collector in the electrode, which is worsened upon cycling due to electronic isolation from cathode particle cracking.<sup>30,54–56</sup> This resistance, acquired from the circuit model fitting, is denoted as contact resistance ( $R_{\text{con}}$ ) and is plotted for each sample in Figure 4a. Over the course of 300 cycles, NM70, NMC70, and NMA70 exhibit an increase in  $R_{\text{con}}$  by, respectively, 64.4, 15.2, and 43.6  $\Omega \text{ cm}^2$ .

After the 4<sup>th</sup> cycle, there is little mechanical strain exerted on the cathode. This strain accumulates and worsens with continued cycling, and eventually can lead to poor conductive adhesion, or contact loss, throughout the cathode bulk and can also contribute to the large initial voltage drops from the 100<sup>th</sup> – 300<sup>th</sup> cycles seen in Figure 3f for NM70. For NM70, the inherently poorer conductivity and structural stability without the influence of a stabilizing dopant, such as Al or Co, compared to NMA70 or NMC70 will exacerbate the deteriorating adhesion and will lead to a larger contact resistance.

An advantage of NMC and NCA cathodes is the presence of Co as it intrinsically promotes good electronic conductivity throughout the cathode and is redox active alongside Ni.<sup>1,57,58</sup> This can explain the much larger  $R_{\text{con}}$  increases present for NM70 and NMA70 as both materials are free of cobalt and are rich in electrochemically inactive Mn and Al compared to the minimal  $R_{\text{con}}$

growth observed with NMC70. In fact, this phenomenon is also seen and addressed in our group's recent article on NMA with 90% Ni content, where we show that NMA had the largest contact resistance among all its Co-containing peers, even though it had the best overall cycling performance.<sup>30</sup> Another recent study details the effects of calendaring on cycling performance, and shows that calendaring of NMA cathodes helps reduce the electrode porosity and thus the first semicircle impedance to match that of its NCM and NCA counterparts, due to the improved interparticle conductive contact throughout the electrode bulk.<sup>59</sup> These findings indicate that the first semicircle impedance can be greatly reduced with sufficient calendaring alone, without any modification of the cathode surface and emphasize that the impedance is largely due to the poor cathode matrix conductivity and not so much due to surface film resistance as previously thought. Additionally, the results highlight the importance of calendaring Co-free cathodes in the future to minimize contact resistance and resulting capacity fade.

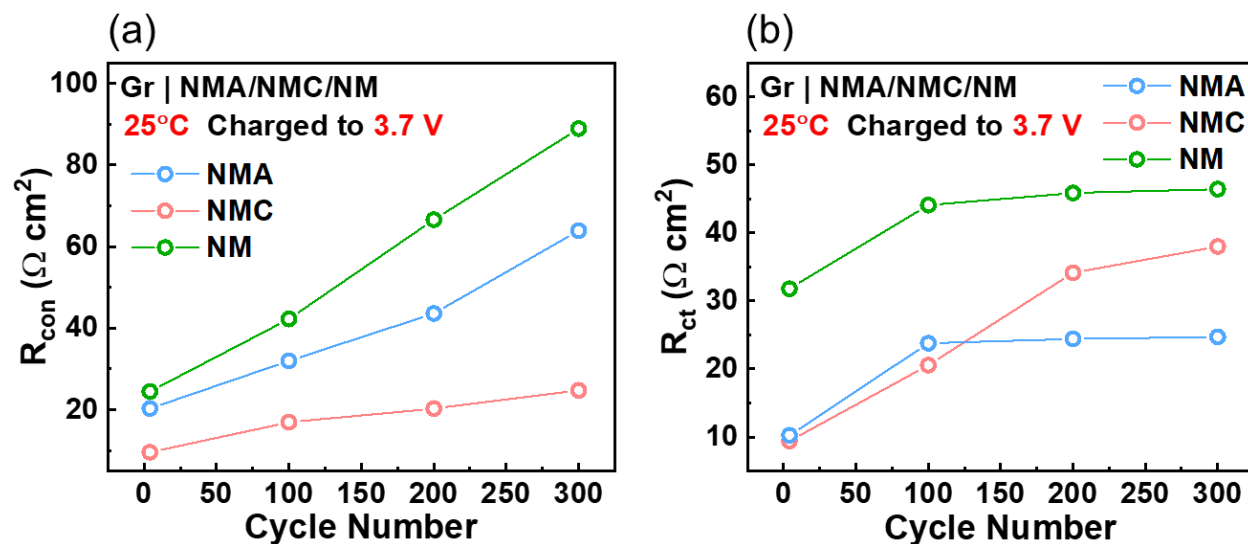


**Figure 4.** Evolutions of (a) contact resistance ( $R_{con}$ ) and (b) charge-transfer resistance ( $R_{ct}$ ) that were fit with an equivalent circuit model of the EIS data of the NMA70, NMC70, and NM70 full cells, measured at the 4<sup>th</sup>, 100<sup>th</sup>, 200<sup>th</sup>, and 300<sup>th</sup> cycles.

Meanwhile, the second semicircle in the impedance spectra in the medium-to-low frequency regime is attributed to the charge-transfer resistance ( $R_{ct}$ ) across the electrode-electrolyte interfaces.<sup>50,60–62</sup> The  $R_{ct}$  values over the course of 300 cycles are plotted and displayed for each sample in Figure 4b. Unlike the first semicircle, this charge-transfer resistance is not due to the intrinsic properties of the electrode materials, such as conductivity, but more so to the kinetic hindrances of the electrode surface reactions due to cathode-electrolyte interface (CEI) and anode SEI formations, and thus is a better indicator of electrode surface film growth.<sup>30,40</sup> Surprisingly, NMC70 displays the greatest increase in  $R_{ct}$  of  $28.6 \Omega \text{ cm}^2$  after cycling. Both NM70 and NMA70 show milder  $R_{ct}$  growths of  $14.5 \Omega \text{ cm}^2$ . However, the initial values of  $R_{ct}$  for both NMA70 and NMC70 being, respectively,  $10.2$  and  $9.4 \Omega \text{ cm}^2$  are much smaller than that of NM70 with  $31.8 \Omega \text{ cm}^2$ . Parallels can be drawn with such a high initial resistance and with the large starting voltage polarization for NM70 shown in Figure S7c, calculated by the difference between the charge and discharge operating voltages. The NM70 cell exhibits a much larger initial polarization compared with that of NMA70 and NMC70, which can be indicative of the poor electrochemical kinetics discussed previously with Figure 3. NMC70, albeit with its greatly reduced  $R_{con}$ , shows a moderate growth in its  $R_{ct}$ , while NMA70 displays the smallest increase in magnitude. The  $R_{ct}$  contributions in the NMC70 and NM70 cells are, respectively, about 1.5x to 2x that of NMA70 after 300 cycles.

The general trend of the total impedance growth over 300 cycles for the three samples are in the increasing order of NMC70 < NMA70 < NM70. Although NMA70 is shown to have a larger growth in  $R_{con}$ , its smaller increase in  $R_{ct}$  compared to that of both NM70 and NMC70 indicates there are less kinetic hindrances across the electrode-electrolyte interfaces. Also, as previously mentioned, the overall cycling decay of NM70 shown back in Figure 3e is less than that of NMA70 or NMC70 as the lithium utilization is lower, but the poor adhesion and surface impedance

buildups for NM70 as depicted in the initial voltage drops and total impedance over many cycles still indicate that these problems are not worthy tradeoffs for slightly less capacity fade. The lower capacity of NM70 during cycling also deems it unfavorable as a high-energy-density cathode. Many convoluting factors influencing the overall impedance growth are clearly at play, but the beneficial effects of Al in mitigating such growth are still demonstrated.<sup>43,63</sup> Lastly, the results illustrate the importance of engineering high-quality electrodes. Processing techniques, such as heated calendaring and planetary vacuum mixing of cathode slurries, can improve the dispersion of slurry additives, such as carbon black, and enhance the mechanical properties of the electrodes.<sup>59</sup> Such methods will help strengthen electrode adhesion and mitigate impedance and polarization growth.

The disparities seen with the impedance spectra indicate that different electrode-electrolyte interfacial reactions are occurring among the three samples during cycling. To better understand the interface chemistry, XPS was utilized on the cathodes of each full cell after long-term cycling. Figure 5a illustrates the C 1s and O 1s spectra from XPS carried out on the cycled cathodes. Among the three, NM70 and NMA70 both possess similarly low intensity ratios of the C-C/C-H bonding peak to the C-O peak in the C 1s spectra, indicating relatively thicker CEIs compared to that of NMC70 that are rich with C-O compounds such as carbonate-based electrolyte decomposition products and other related organic species.<sup>64</sup> Figure 5c shows the atomic compositions of the main CEI and SEI components from XPS results (see Table S4 for tabulated data). Based on the percentages, NMA70 has a larger C content compared to NM70, which may indicate a larger amount of organic C-containing electrolyte species on NMA70. However, the contribution is also from the increased C-C/C-H bonding peak intensity for NMA70, which is characteristic of

conductive carbon black in the bulk cathode, suggesting that a slightly thinner CEI is formed on NMA70 since there is more carbon black exposed near the surface.<sup>65</sup>

The O 1s spectra of NMA70 display a higher intensity M-O peak compared to NM70, pertaining to the transition-metal oxide bulk near the surface, which also supports the implication of a thinner CEI development compared to that in NM70.<sup>66,67</sup> NMC70 yields the strongest M-O peak signal suggesting that it has the least amount of electrolyte species deposited on the cathode surface and, therefore, the thinnest CEI. This is further indicated by the smallest C/O ratio in the NMC70 CEI as shown in Figure 5c. Most C and O-related species seen in the XPS data are from electrolyte solvent decomposition, except for one O signal coming from the M-O peak. Given that most of the C and O electrolyte species among the three CEIs are similar, the largest M-O signal in NMC70 would accordingly bring down the C/O ratio as seen and serves as an alternative way of identifying the CEI thickness.

The F 1s spectra of the cathodes provided in Figure S8 further reveal the worsened electrolyte degradation products forming on the NM70 CEI compared to the other two, as it has the largest  $\text{Li}_x\text{PO}_y\text{F}_z/\text{Li}_x\text{PF}_y$  peak, which are species formed from  $\text{LiPF}_6$  salt decomposition.<sup>5,68</sup> This is better signified in Figure 5c, which shows that the NM70 CEI is comprised of the largest amounts of F and P elements, while the NMA70 CEI has the smallest compositions. Additional discussion on the electrolyte decomposition species contributing to the XPS results are provided in the supporting note below Figure S8. Overall, the XPS data of the cycled cathodes holistically show that NMC70 has the thinnest CEI architecture whereas NM70 yields the thickest that is concentrated with electrolyte decomposition species, while NMA70 follows somewhere in between.

Alongside the cathodes, the cycled graphite anodes are also analyzed through XPS in order to probe the SEI species to gain an inclusive understanding of surface degradations on both electrodes. Based on the C 1s spectra in Figure 5b, the anode from the NMA70 cell has a relatively lower C-C/C-H peak to those from both the NM70 and NMC70 cells. Additionally, all three anode samples have similar intensities of the C-O and C=O peaks. These results signify that the graphite anode from the NMA70 cell has the most organic C-O and C=O species that passivate the SEI, which are artifacts from electrolyte solvent reduction reactions that mask the carbon black peak intensity.<sup>69</sup> The graphite anode from the NM70 cell, meanwhile with the greatest C-C/C-H peak intensity, has the least amount of organic species that comprise the SEI. This is supported based on Figure 5c, which shows that the graphite anode SEI from the NMA70 cell has the smallest C/O ratio of all the three anodes. All O-containing species are largely from the organic electrolyte decomposition products, and all but one C-containing species (C-C/C-H peak indicative of conductive carbon black), are of the same based on the anode C1s and O1s spectra. Therefore, a smaller C/O ratio thus implies a larger SEI composition that is rich in organic electrolyte components.

The F 1s spectra for the anodes, however, illustrate that the graphite from the NM70 cell has the largest  $\text{Li}_x\text{PO}_y\text{F}_z/\text{Li}_x\text{PF}_y$  and  $\text{LiF}/\text{MF}_x$  peaks, indicative of the most severe  $\text{LiPF}_6$  salt decomposition and transition-metal dissolution and migration onto the anode.<sup>70,71</sup> Despite having the thinnest CEI, the NMC70 cell displays moderate intensities for its graphite anode F 1s peaks, while the graphite from the NMA70 cell yields the smallest overall peaks, implying it has the least degradation among the three anodes.<sup>72</sup> This is further showcased in Figure 5c, as the graphite anode from the NMA70 cell has the smallest F and P atomic compositions among the three samples. The O 1s spectra given in Figure S8 indicate analogous C-O and C=O peak intensities for all anodes.

The anode XPS data make it apparent that there are two extremes in terms of the SEI composition. On one end, the anode SEI is rich in organic species stemming from electrolyte solvent reduction products as seen with the graphite from the NMA70 cell. On the other end, the SEI is dominated by transition-metal and Li crossover products as seen with the graphite from the NM70 cell, leaving the anode SEI from the NMC70 cell composed of both species to intermediate extents.

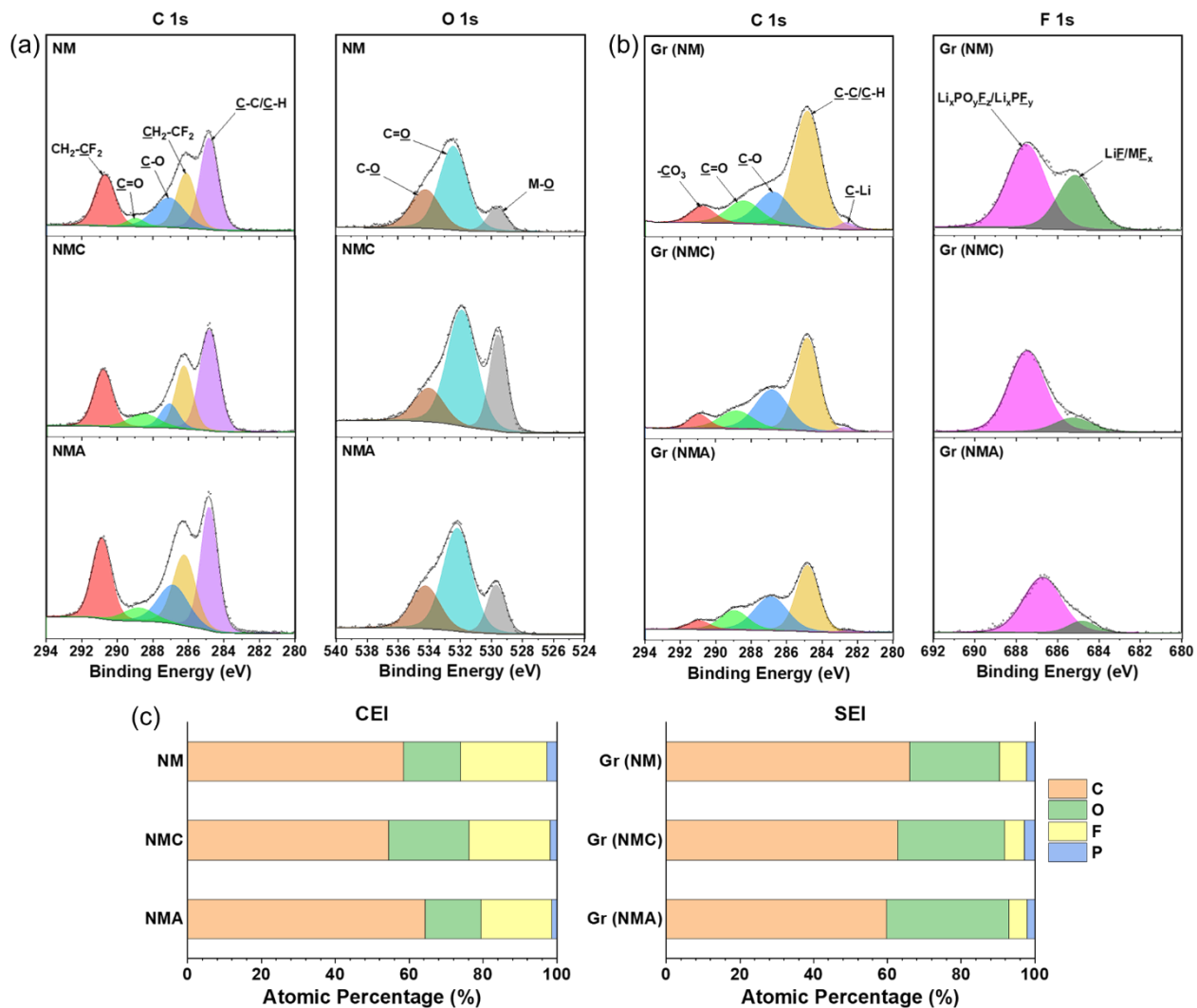


**Figure 5.** XPS data: (a) C 1s and O 1s spectra of the cycled NMA70, NMC70, and NM70 cathodes, along with the (b) C 1s and F 1s spectra of the cycled graphite anodes, as well as the (c) atomic concentrations of the main elements comprising the CEI and SEI layers.

Comprehensively, the severity of CEI and SEI degradation among the three cells is in the decreasing order of NM70 > NMA70 > NMC70 for the CEI and NM70 > NMC70 > NMA70 for the graphite SEI. NM70, given its thickest CEI with organic and Li salt species and the worst SEI passivation on the graphite paired with it due to transition-metal dissolution, suffers from the worst overall electrode-electrolyte interface degradation. Studies have shown that a large contribution to SEI degradation is the surface film growth near the anode-separator interface, which is caused by cathode transition-metal dissolution and crossover to the anode surface, particularly due to manganese. This in turn will greatly compromise the SEI passivation and hinder ion transport throughout the anode.<sup>63,70,73</sup> As NM70 contains the most manganese-rich composition with no other stabilizing transition metal, such as cobalt or aluminum, it is logical to visualize from the results that it suffers from the worst dissolution and passivation on the anode side. This is supported with Figure S9, which pictures the disassembled graphite anodes after long-term cycling in full cells prior to XPS testing. The anode paired with NM70 clearly portrays the worst SEI deterioration most likely from transition-metal dissolution. Previous studies have also shown that these deposited transition-metal species on the graphite anode can induce catalytic formation of metallic Li microstructures on the graphite surface, largely in the form of Li dendrites, and can compromise safety and capacity fading.<sup>74</sup> The NMC70-paired graphite also shows small spots near the center of the anode, indicating some mild deterioration, while the anode paired with NMA70 shows no noticeable degradation compared to the two. The anode surface compositions of the three cells also suggest that the organic species growth on the SEI does not seem to exacerbate the impedance to the extent of the deposited transition-metal species.

The impact of TM dissolution can be seen in Figure S10, which shows the charge-discharge curves of an additional C/10 cycle that was done after the main 300 cycles finished for each full

cell. This cycle is referred to as a reactivation cycle. NM70 has the lowest CE following reactivation and the largest capacity drop from its final 1C discharge capacity of 130 mA h g<sup>-1</sup> after 300 cycles to 117 mA h g<sup>-1</sup> after the C/10 reactivation cycle. NMA70, however, has a higher CE and presents a capacity increase from its 1C discharge capacity of 155 mA h g<sup>-1</sup> to its reactivation cycle capacity of 165 mA h g<sup>-1</sup>. NMC70 also has a similar CE to that of NMA70 and a smaller capacity decrease from its 1C capacity to its reactivation capacity. This suggests that NM70 may be on the verge of dissolution-induced rollover failure.<sup>75,76</sup>

One of the notable problems with high-Ni cathodes is the reduction of transition-metal species and oxygen loss in the surface during cycling, especially at high voltages. This leads to insulating rock-salt formation mainly in the form of NiO, which is exacerbated by initial Li/Ni mixing and transition-metal dissolution.<sup>77</sup> Therefore, in addition to XPS, high-angle annular dark-field scanning transmission electron microscopy (HAADF-STEM) imaging and electron energy loss spectroscopy (EELS) were carried out on the three cathode samples in order to probe the degradation depth of reduced transition-metal species from the surface to bulk. HAADF-STEM images in Figures 6a-c qualitatively show the extent of such surface degradation in the cycled cathodes, with NM70 exhibiting a significantly larger degradation depth over twice the thickness to those of NMA70 and NMC70. O-K edge EELS line scans were performed along the surface to bulk lines indicated in the HAADF-STEM images to quantify the depth of rock-salt and other reduced transition-metal oxide phases as shown in Figure 6d. Layered oxides have distinct O-K pre-edge peaks (~528 eV) and O-K main-edge peaks (~ 540 eV) which correspond, respectively, to the transition of electrons in the O 1s orbital to the O 2p-TM 3d and O 2p-TM 4sp hybridized orbital states. A lower O-K pre-edge peak intensity indicates more oxygen deficiency and transition-metal reduction.<sup>78</sup> The EELS line scans in Figure 6d portray the various depths at which

the O-K pre-edge peak intensities began to strongly manifest, which reveal the point at which the bulk layered oxide structure is reached. NMA70 and NMC70 reach strong O-K pre-edge intensities, respectively, at around 8 nm and 7 nm scanning depths, implying that these are the thicknesses of rock-salt and other reduced transition-metal phases stemming from the surface to the layered oxide bulk. NM70 reaches strong pre-edge intensity peaks at around an 18 nm scanning depth, supporting the observations made in Figures 6a-c about it having the greatest degradation depth among the three samples.

Moreover, the energy difference between the O-K main-edge and pre-edge ( $\Delta E$ ) gives quantitative information of the Ni oxidation state. A larger  $\Delta E$  value indicates a higher oxidation state of Ni bound to oxygen, while a lower  $\Delta E$  indicates a more reduced Ni oxidation state.<sup>79,80</sup> Figure 6e shows the evolution of  $\Delta E$  over the course of the EELS line scanning depths for the three cathodes. NMA70 and NMC70 initially have lower  $\Delta E$  values around 9 eV and reach plateaus at, respectively, 7.5 nm and 7 nm, indicating that the bulk layered structure is reached and further supports the results in Figure 6d. Likewise, NM70 shows a delayed increase in  $\Delta E$ , starting at around 8 eV and reaching a plateau at 18 nm. The severe rock-salt formation and degradation from the cathode surface to bulk of NM70 compared to those of NMA70 and NMC70 compliments the conclusions reached from the XPS results and can explain its thickest CEI formation. The greater extent of degradation and reduction of NM70 also elucidates the consequential transition-metal dissolution and crossover to the graphite anode and further bolsters the stabilizing effect of Al in mitigating such phenomena with NMA70, as previously discussed.

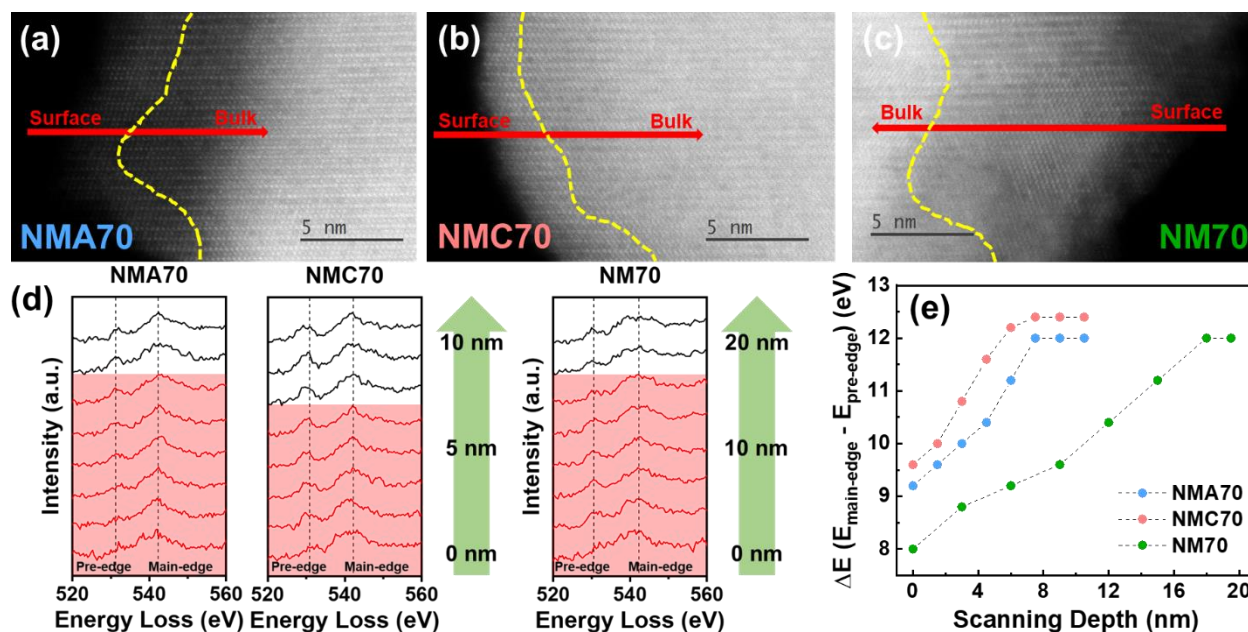


Figure 6. HAADF-STEM images of (a) NMA70, (b) NMC70, and (c) NM70 cathodes after 300 cycles. (d) EELS O-K edge spectra of the cathodes from the surface to bulk. (e) Evolution of  $\Delta E$  of the O-K edges of the cathodes.

Overall, the detrimental impedance growth and CEI buildup coupled with the worst resulting SEI degradation of NM70 seen with EIS, XPS, and TEM data indicate the vulnerability of electrode materials, especially during high-voltage operation. The NMC70 full cell experienced milder anode degradation and had the best CEI passivation, whereas the NMA70 full cell had the least chemical crossover to the anode while tolerating moderate CEI growth on the cathode. The benefits of Al in NMA70 are showcased here with its reduced charge-transfer resistance, as Al incorporation into the layered structure is known to suppress transition-metal dissolution and subsequent chemical crossover to the anode during cycling due to the stronger transition metal-oxygen bond strength, which perturbs structural changes throughout the lattice.<sup>29,63</sup> The fact that NMA70 is plagued by higher total impedance and CEI growth compared to NMC70, yet can still deliver nearly equivalent capacities and cyclability with it, indicates the potential space for

optimization that can be made to further mitigate capacity loss from this material and boost its practicality in the LIB market.

To further assess the surface stabilities of the cathodes, self-discharge experiments were conducted in which Li-metal half cells of each cathode were charged to 4.5 V at a C/10 rate, left to rest for four days at 50°C in order to observe the open-circuit voltage (OCV) decay, then discharged to 2.8 V. The phenomena of OCV decay at high voltages is caused by active Li<sup>+</sup> loss due to severe electrolyte oxidation reactions at the cathode surface, all of which worsen with increasing temperature.<sup>81</sup> Therefore, the cathode with the highest OCV retention would indicate the most stable surface. During the charging step as shown in Figure 7, NM70 still displays a noticeably higher voltage shoulder at around 3.7 V compared to 3.6 V for both NMA70 and NMC70. After resting for four days following the charge step to 4.5 V, NMA70 possesses a higher OCV retention of 4.20 V, while both NMC70 and NM70 exhibit worse OCV decays to, respectively, 4.05 V and 4.00 V. Upon discharging, NMA70 displays the largest capacity of 160 mA h g<sup>-1</sup>, followed by NMC70 and NM70 with, respectively, 155 and 117 mA h g<sup>-1</sup>. The coulombic efficiencies of each cell in Figure 7 were determined by normalizing the discharge capacities by the respective charge capacities prior to high temperature resting. NMA70 and NMC70 have very similar CEs of, respectively, 64% and 65% while NM70 presents the lowest CE with 51%.

The worst OCV decay and CE of NM70 confirms the results discussed from the XPS and TEM sections on the poor CEI stability and decomposition products that result in active material loss. During the rest step at a high voltage of 4.5 V, the thickening of the CEI due to electrolyte oxidation is likely to occur and will most definitely be exacerbated at an increased temperature of 50°C. Interestingly, the self-discharge results revealed that NMA70 has less OCV decay compared

to NMC70 yet has a marginally lower CE. This suggests that the benefits of Al on improving the overall interfacial stability are more pronounced at higher operating temperatures given with the mitigated OCV decay, but the effects of the robust CEI stability in NMC70 as indicated in the XPS results persist as well.

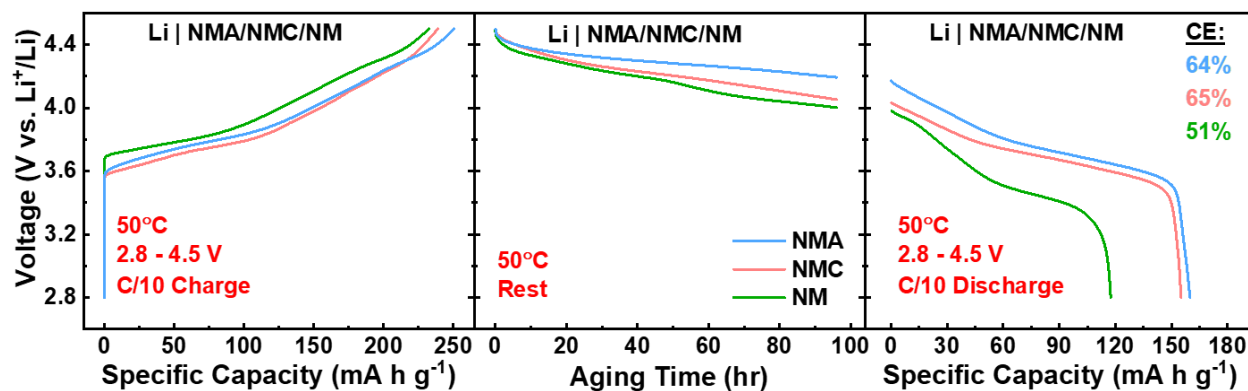


**Figure 7.** Self-discharge profiles of NMA70, NMC70, and NM70 at 50°C.

**Thermal Stability.** Aside from cycling and interfacial stabilities of high-Ni cathodes, thermal stability is another critical factor to consider for developing safer EV batteries. At high states of charge (SoC), layered-oxide cathodes are prone to undergo phase transformations to spinel and rock-salt phases, which involve the release of oxygen gas. The gas will react with the electrolyte and lithiated graphite anodes in highly exothermic reactions, which will lead to thermal runaway and ultimately battery fires and explosions.<sup>82,83</sup> DSC experiments were carried out to thus gauge the thermal abuse tolerances of the cathodes at high SoCs. All three cathodes were charged to 80% SoC to ensure an identical state of delithiation. Figure 8 depicts the various peak temperatures and total heat released determined using the integral range from 160 to 310 °C, as indicated by dashed lines for each cathode upon reacting with the electrolyte.

NM70 shows the earliest exothermic peak temperature of 225 °C, even earlier than that of NMC70 with 232 °C. Since NM70 was shown to have the lowest charge capacity as indicated in Figure 3, it had to be charged to a higher voltage state in order to reach an SoC identical with those of NMC70 and NMA70. This could induce an earlier initiation for phase transformations and coupled oxygen release with increasing temperatures and could explain it having a sooner onset temperature. However, NM70 interestingly displays a slightly smaller total heat release of 658 J g<sup>-1</sup> compared with 661 J g<sup>-1</sup> for NMC70, indicating that larger Mn incorporation may alleviate the heat generation from cathodes.<sup>23</sup> Additionally, a miniature shoulder peak at around 200 °C is seen for NM70 before the main peak, which could be indicative of small exothermic reactions between the released oxygen from the cathode lattice and electrolyte that occur prior to the main exothermic event. Earlier investigations explain that such peaks form when nearing the onset temperature for the *R-3m* layered to *Fd3m* cubic spinel phase transition.<sup>84,85</sup> The absence of such peaks for NMC70 and NMA70 possibly implies different effects of Co and Al in governing exothermic activity in Ni-based cathodes. NMA70 has superior thermal stability compared to both cathodes, with a higher peak temperature and a smaller total heat generation of, respectively, 253 °C and 646 J g<sup>-1</sup>. The delayed peak onset and reduced heat for NMA70 indicates the beneficial impact of Al on greatly improving the thermal stability of the cathode and confirms the results found in previous studies.<sup>7,29,86</sup>

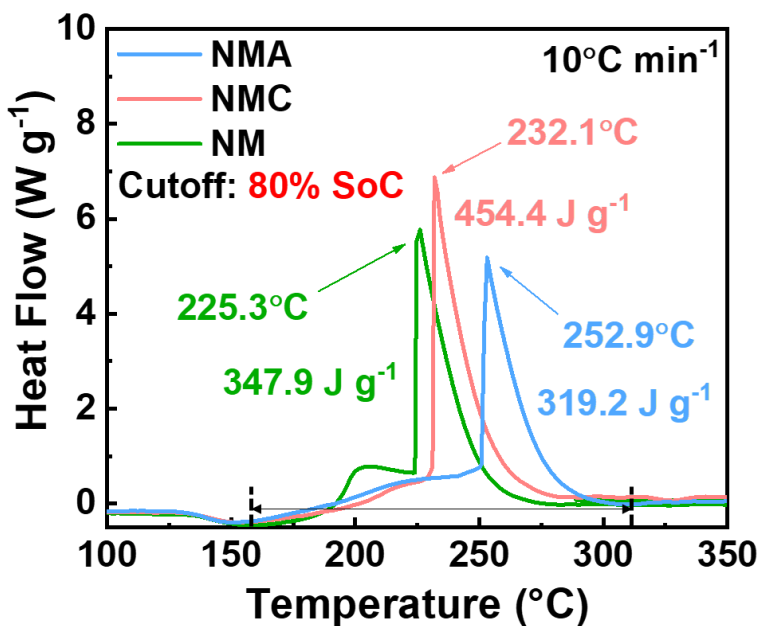


**Figure 8.** DSC profiles of the cathodes charged to 80% SoC ( $\sim 220 \text{ mA h g}^{-1}$ ) in half cells with Li-metal anode.

## Conclusion

In this work, we introduce a novel high-nickel NMA composition  $\text{LiNi}_{0.7}\text{Mn}_{0.25}\text{Al}_{0.05}\text{O}_2$  and benchmark how it performs relative to its cobalt-bearing  $\text{LiNi}_{0.7}\text{Mn}_{0.15}\text{Co}_{0.15}\text{O}_2$  counterpart as well as Co- and Al-free  $\text{LiNi}_{0.7}\text{Mn}_{0.3}\text{O}_2$  in order to discern the effects of Mn, Al, and Co in high-Ni cathodes. The benefits of Al doping are shown with a striking increase in the specific capacity of NMA70, surprisingly matching that of NMC70, and a stabilized high-voltage cycling performance compared to those of both NMC70 and NM70 in full cells. EIS curves show the smallest charge-transfer impedance growth for NMA70 after full cell cycling amongst the tested cathodes. XPS analyses further indicate the smallest concentrations of metal fluoride-based species on the anode, indicating that NMA70 exhibits the highest stability and greatest suppression of chemical crossover to the corresponding graphite anode during full cell cycling. TEM analyses compliment the previous results by showing mitigated rock-salt formation and overall phase degradation for

NMA70 compared to NM70. The robustness of the transition-metal layer after Al incorporation is also shown through high-temperature self-discharge tests in which the NMA70 cathode yields the smallest OCV decay, along with the best thermal stability shown with the highest exothermic peak temperature through DSC experiments.

Looking forward, it is hoped that this work provides a path towards reducing Co from current commercial high-Ni layered-oxide cathodes by continuing to explore the different compositions of the NMA cathode class. Future focus towards understanding the degradation mechanisms governing air stability as well as thermal stability of Co-free cathodes will be of particular importance in order to boost the practicality of these materials for the EV industry. Holistically, understanding the roles of Co-alternative dopants in high-Ni cathodes will be what ultimately dictates the feasible incorporation of these materials into LIBs for next-generation EVs.

### **Associated Content**

**Supporting Information.** SEM images, additional electrochemical test results (coulombic efficiency, voltage profiles,  $dQ\ dV^{-1}$  curves, capacity checks, EIS plots, polarization growth), images of cycled graphite anodes, XPS results, and Rietveld refinement results.

### **Author Information**

Corresponding Author

\*E-mail: manth@austin.utexas.edu

### **Notes**

The authors declare that two of the authors (Wangda Li and Arumugam Manthiram) are co-founders of TexPower, a startup company focusing on cobalt-free cathode materials for lithium-ion batteries.

## **Acknowledgements**

The authors acknowledge the support from the Assistant Secretary for Energy Efficiency and Renewable Energy, Office of Vehicle Technologies of the U.S. Department of Energy (award number DE-EE0008445). The authors would like to acknowledge Drs. Eunmi Jo and Karalee Jarvis for their assistance with TEM characterization and analysis as well as Dr. Hugo Celio for his help with XPS characterization.

## References

- (1) Manthiram, A. A Reflection on Lithium-Ion Battery Cathode Chemistry. *Nat Commun* 2020, *11* (1), 1550. <https://doi.org/10.1038/s41467-020-15355-0>.
- (2) Li, W.; Erickson, E. M.; Manthiram, A. High-Nickel Layered Oxide Cathodes for Lithium-Based Automotive Batteries. *Nat Energy* 2020, *5* (1), 26–34. <https://doi.org/10.1038/s41560-019-0513-0>.
- (3) Goodenough, J. B.; Kim, Y. Challenges for Rechargeable Li Batteries. *Chem Mater* 2010, *22* (3), 587–603. <https://doi.org/10.1021/cm901452z>.
- (4) Mizushima, K.; Jones, P. C.; Wiseman, P. J.; Goodenough, J. B.  $\text{Li}_x\text{CoO}_2$  ( $0 < x < 1$ ): A New Cathode Material for Batteries of High Energy Density. *Mater Res Bull* 1980, *15* (6), 783–789. [https://doi.org/10.1016/0025-5408\(80\)90012-4](https://doi.org/10.1016/0025-5408(80)90012-4).
- (5) Li, W.; Dolocan, A.; Oh, P.; Celio, H.; Park, S.; Cho, J.; Manthiram, A. Dynamic Behaviour of Interphases and Its Implication on High-Energy-Density Cathode Materials in Lithium-Ion Batteries. *Nat Commun* 2017, *8* (1), 14589. <https://doi.org/10.1038/ncomms14589>.
- (6) Li, M.; Lu, J. Cobalt in Lithium-Ion Batteries. *Science* 2020, *367* (6481), 979–980. <https://doi.org/10.1126/science.aba9168>.
- (7) Li, H.; Cormier, M.; Zhang, N.; Inglis, J.; Li, J.; Dahn, J. R. Is Cobalt Needed in Ni-Rich Positive Electrode Materials for Lithium Ion Batteries? *J Electrochem Soc* 2019, *166* (4), A429–A439. <https://doi.org/10.1149/2.1381902jes>.
- (8) U.S. DRIVE Electrochemical Energy Storage Technical Team Roadmap. <https://www.osti.gov/biblio/1220126> (accessed 2021-09-01).
- (9) Manthiram, A.; Knight, J. C.; Myung, S.; Oh, S.; Sun, Y. Nickel-Rich and Lithium-Rich Layered Oxide Cathodes: Progress and Perspectives. *Adv Energy Mater* 2015, *6* (1), 1501010. <https://doi.org/10.1002/aenm.201501010>.
- (10) Liu, W.; Oh, P.; Liu, X.; Lee, M.; Cho, W.; Chae, S.; Kim, Y.; Cho, J. Nickel-Rich Layered Lithium Transition-Metal Oxide for High-Energy Lithium-Ion Batteries. *Angewandte Chemie Int Ed* 2015, *54* (15), 4440–4457. <https://doi.org/10.1002/anie.201409262>.
- (11) Zou, Y.-G.; Meng, F.; Xiao, D.; Sheng, H.; Chen, W.-P.; Meng, X.-H.; Du, Y.-H.; Gu, L.; Shi, J.-L.; Guo, Y.-G. Stable Interfacial Phase on Single-Crystalline Ni-Rich Cathode via Chemical Reaction with Phosphomolybdic Acid. *Nano Energy* 2021, *87*, 106172. <https://doi.org/10.1016/j.nanoen.2021.106172>.
- (12) Li, X.; Gao, A.; Tang, Z.; Meng, F.; Shang, T.; Guo, S.; Ding, J.; Luo, Y.; Xiao, D.; Wang, X.; Su, D.; Zhang, Q.; Gu, L. Robust Surface Reconstruction Induced by Subsurface Ni/Li

Antisites in Ni-Rich Cathodes. *Adv Funct Mater* 2021, 2010291.  
<https://doi.org/10.1002/adfm.202010291>.

(13) Manthiram, A.; Song, B.; Li, W. A Perspective on Nickel-Rich Layered Oxide Cathodes for Lithium-Ion Batteries. *Energy Storage Mater* 2017, 6, 125–139.  
<https://doi.org/10.1016/j.ensm.2016.10.007>.

(14) Kim, J.; Lee, H.; Cha, H.; Yoon, M.; Park, M.; Cho, J. Prospect and Reality of Ni-Rich Cathode for Commercialization. *Adv Energy Mater* 2018, 8 (6), 1702028.  
<https://doi.org/10.1002/aenm.201702028>.

(15) Delmas, C.; Saadoun, I.; Rougier, A. The Cycling Properties of the  $\text{Li}_x\text{Ni}_{1-y}\text{Co}_y\text{O}_2$  Electrode. *J Power Sources* 1993, 44 (1–3), 595–602. [https://doi.org/10.1016/0378-7753\(93\)80208-7](https://doi.org/10.1016/0378-7753(93)80208-7).

(16) Delmas, C.; Ménétrier, M.; Croguennec, L.; Saadoun, I.; Rougier, A.; Pouillier, C.; Prado, G.; Grüne, M.; Fournès, L. An Overview of the  $\text{Li}(\text{Ni},\text{M})\text{O}_2$  Systems: Syntheses, Structures and Properties. *Electrochim Acta* 1999, 45 (1–2), 243–253. [https://doi.org/10.1016/s0013-4686\(99\)00208-x](https://doi.org/10.1016/s0013-4686(99)00208-x).

(17) Radin, M. D.; Hy, S.; Sina, M.; Fang, C.; Liu, H.; Vinckeviciute, J.; Zhang, M.; Whittingham, M. S.; Meng, Y. S.; Ven, A. V. der. Narrowing the Gap between Theoretical and Practical Capacities in Li-Ion Layered Oxide Cathode Materials. *Adv Energy Mater* 2017, 7 (20), 1602888. <https://doi.org/10.1002/aenm.201602888>.

(18) Wang, X.; Ding, Y.; Deng, Y.; Chen, Z. Ni-Rich/Co-Poor Layered Cathode for Automotive Li-Ion Batteries: Promises and Challenges. *Adv Energy Mater* 2020, 10 (12), 1903864.  
<https://doi.org/10.1002/aenm.201903864>.

(19) Sharma, S. S.; Manthiram, A. Towards More Environmentally and Socially Responsible Batteries. *Energ Environ Sci* 2020, 13 (11), 4087–4097. <https://doi.org/10.1039/d0ee02511a>.

(20) Olivetti, E. A.; Ceder, G.; Gaustad, G. G.; Fu, X. Lithium-Ion Battery Supply Chain Considerations: Analysis of Potential Bottlenecks in Critical Metals. *Joule* 2017, 1 (2), 229–243.  
<https://doi.org/10.1016/j.joule.2017.08.019>.

(21) Schmuch, R.; Wagner, R.; Hörpel, G.; Placke, T.; Winter, M. Performance and Cost of Materials for Lithium-Based Rechargeable Automotive Batteries. *Nat Energy* 2018, 3 (4), 267–278. <https://doi.org/10.1038/s41560-018-0107-2>.

(22) Kim, Y.; Seong, W. M.; Manthiram, A. Cobalt-Free, High-Nickel Layered Oxide Cathodes for Lithium-Ion Batteries: Progress, Challenges, and Perspectives. *Energy Storage Mater* 2021, 34, 250–259. <https://doi.org/10.1016/j.ensm.2020.09.020>.

(23) Zheng, J.; Kan, W. H.; Manthiram, A. Role of Mn Content on the Electrochemical Properties of Nickel-Rich Layered  $\text{LiNi}_{0.8-x}\text{Co}_{0.1}\text{Mn}_{0.1+x}\text{O}_2$  ( $0.0 \leq x \leq 0.08$ ) Cathodes

for Lithium-Ion Batteries. *Acs Appl Mater Inter* 2015, 7 (12), 6926–6934.  
<https://doi.org/10.1021/acsami.5b00788>.

(24) Hwang, B. J.; Tsai, Y. W.; Chen, C. H.; Santhanam, R. Influence of Mn Content on the Morphology and Electrochemical Performance of  $\text{LiNi}_{1-x-y}\text{Co}_x\text{Mn}_y\text{O}_2$  Cathode Materials. *J Mater Chem* 2003, 13 (8), 1962–1968. <https://doi.org/10.1039/b301468c>.

(25) Wang, D.; Xin, C.; Zhang, M.; Bai, J.; Zheng, J.; Kou, R.; Ko, J. Y. P.; Huq, A.; Zhong, G.; Sun, C.-J.; Yang, Y.; Chen, Z.; Xiao, Y.; Amine, K.; Pan, F.; Wang, F. Intrinsic Role of Cationic Substitution in Tuning Li/Ni Mixing in High-Ni Layered Oxides. *Chem Mater* 2019, 31 (8), 2731–2740. <https://doi.org/10.1021/acs.chemmater.8b04673>.

(26) Liu, T.; Dai, A.; Lu, J.; Yuan, Y.; Xiao, Y.; Yu, L.; Li, M.; Gim, J.; Ma, L.; Liu, J.; Zhan, C.; Li, L.; Zheng, J.; Ren, Y.; Wu, T.; Shahbazian-Yassar, R.; Wen, J.; Pan, F.; Amine, K. Correlation between Manganese Dissolution and Dynamic Phase Stability in Spinel-Based Lithium-Ion Battery. *Nat Commun* 2019, 10 (1), 4721. <https://doi.org/10.1038/s41467-019-12626-3>.

(27) Dianat, A.; Seriani, N.; Bobeth, M.; Cuniberti, G. Effects of Al-Doping on the Properties of Li–Mn–Ni–O Cathode Materials for Li-Ion Batteries: An Ab Initio Study. *J Mater Chem A* 2013, 1 (32), 9273–9280. <https://doi.org/10.1039/c3ta11598d>.

(28) Zhou, K.; Xie, Q.; Li, B.; Manthiram, A. An In-Depth Understanding of the Effect of Aluminum Doping in High-Nickel Cathodes for Lithium-Ion Batteries. *Energy Storage Mater* 2021, 34, 229–240. <https://doi.org/10.1016/j.ensm.2020.09.015>.

(29) Li, W.; Lee, S.; Manthiram, A. High-Nickel NMA: A Cobalt-Free Alternative to NMC and NCA Cathodes for Lithium-Ion Batteries. *Adv Mater* 2020, 32 (33), 2002718. <https://doi.org/10.1002/adma.202002718>.

(30) Lee, S.; Li, W.; Dolocan, A.; Celio, H.; Park, H.; Warner, J. H.; Manthiram, A. In-Depth Analysis of the Degradation Mechanisms of High-Nickel, Low/No-Cobalt Layered Oxide Cathodes for Lithium-Ion Batteries. *Adv Energy Mater* 2021, 2100858. <https://doi.org/10.1002/aenm.202100858>.

(31) Nichols, A. R.; Walton, J. H. The Autoxidation of Manganous Hydroxide. *J Am Chem Soc* 1942, 64 (8), 1866–1870. <https://doi.org/10.1021/ja01260a034>.

(32) Toby, B. H.; Dreele, R. B. V. GSAS-II: The Genesis of a Modern Open-Source All Purpose Crystallography Software Package. *J Appl Crystallogr* 2013, 46 (2), 544–549. <https://doi.org/10.1107/s0021889813003531>.

(33) Lamb, J.; Manthiram, A. Synthesis Control of Layered Oxide Cathodes for Sodium-Ion Batteries: A Necessary Step Toward Practicality. *Chem Mater* 2020, 32 (19), 8431–8441. <https://doi.org/10.1021/acs.chemmater.0c02435>.

- (34) Dogan, F.; Vaughey, J. T.; Iddir, H.; Key, B. Direct Observation of Lattice Aluminum Environments in Li Ion Cathodes  $\text{LiNi}_{1-y-z}\text{Co}_y\text{Al}_z\text{O}_2$  and Al-Doped  $\text{LiNi}_x\text{Mn}_y\text{Co}_z\text{O}_2$  via  $^{27}\text{Al}$  MAS NMR Spectroscopy. *Acs Appl Mater Inter* 2016, 8 (26), 16708–16717. <https://doi.org/10.1021/acsami.6b04516>.
- (35) Jia, G.; Liu, S.; Yang, G.; Li, F.; Wu, K.; He, Z.; Shangguan, X. The Multiple Effects of Al-Doping on the Structure and Electrochemical Performance of  $\text{LiNi}_{0.5}\text{Mn}_{0.5}\text{O}_2$  as Cathode Material at High Voltage. *Ionics* 2018, 24 (12), 3705–3715. <https://doi.org/10.1007/s11581-018-2553-z>.
- (36) Zhang, B.; Chen, G.; Xu, P.; Li, C. C. Effect of Equivalent and Non-Equivalent Al Substitutions on the Structure and Electrochemical Properties of  $\text{LiNi}_{0.5}\text{Mn}_{0.5}\text{O}_2$ . *J Power Sources* 2008, 176 (1), 325–331. <https://doi.org/10.1016/j.jpowsour.2007.10.043>.
- (37) Myung, S.-T.; Komaba, S.; Hirosaki, N.; Hosoya, K.; Kumagai, N. Improvement of Structural Integrity and Battery Performance of  $\text{LiNi}_{0.5}\text{Mn}_{0.5}\text{O}_2$  by Al and Ti Doping. *J Power Sources* 2005, 146 (1–2), 645–649. <https://doi.org/10.1016/j.jpowsour.2005.03.083>.
- (38) Mesnier, A.; Manthiram, A. Synthesis of  $\text{LiNiO}_2$  at Moderate Oxygen Pressure and Long-Term Cyclability in Lithium-Ion Full Cells. *Acs Appl Mater Inter* 2020, 12 (47), 52826–52835. <https://doi.org/10.1021/acsami.0c16648>.
- (39) Li, H.; Zhang, N.; Li, J.; Dahn, J. R. Updating the Structure and Electrochemistry of  $\text{Li}_x\text{NiO}_2$  for  $0 \leq x \leq 1$ . *J Electrochem Soc* 2018, 165 (13), A2985–A2993. <https://doi.org/10.1149/2.0381813jes>.
- (40) Li, J.; Harlow, J.; Stakheiko, N.; Zhang, N.; Paulsen, J.; Dahn, J. Dependence of Cell Failure on Cut-Off Voltage Ranges and Observation of Kinetic Hindrance in  $\text{LiNi}_{0.8}\text{Co}_{0.15}\text{Al}_{0.05}\text{O}_2$ . *J Electrochem Soc* 2018, 165 (11), A2682–A2695. <https://doi.org/10.1149/2.0491811jes>.
- (41) Hong, C.; Leng, Q.; Zhu, J.; Zheng, S.; He, H.; Li, Y.; Liu, R.; Wan, J.; Yang, Y. Revealing the Correlation between Structural Evolution and Li<sup>+</sup> Diffusion Kinetics of Nickel-Rich Cathode Materials in Li-Ion Batteries. *J Mater Chem A* 2020, 8 (17), 8540–8547. <https://doi.org/10.1039/d0ta00555j>.
- (42) Hou, P.; Li, F.; Sun, Y.; Pan, M.; Wang, X.; Shao, M.; Xu, X. Improving Li<sup>+</sup> Kinetics and Structural Stability of Nickel-Rich Layered Cathodes by Heterogeneous Inactive- $\text{Al}^{3+}$  Doping. *Acs Sustain Chem Eng* 2018, 6 (4), 5653–5661. <https://doi.org/10.1021/acssuschemeng.8b00909>.
- (43) Zhang, C.; Wan, J.; Li, Y.; Zheng, S.; Zhou, K.; Wang, D.; Wang, D.; Hong, C.; Gong, Z.; Yang, Y. Restraining the Polarization Increase of Ni-Rich and Low-Co Cathodes upon Cycling by Al-Doping. *J Mater Chem A* 2020, 8 (14), 6893–6901. <https://doi.org/10.1039/d0ta00260g>.

- (44) Zhang, B.; Chen, G.; Liang, Y.; Xu, P. Structural and Electrochemical Properties of  $\text{LiNi}_{0.5}\text{Mn}_{0.5-x}\text{Al}_x\text{O}_2$  ( $X=0, 0.02, 0.05, 0.08,$  and  $0.1$ ) Cathode Materials for Lithium-Ion Batteries. *Solid State Ionics* 2009, *180* (4–5), 398–404. <https://doi.org/10.1016/j.ssi.2009.01.009>.
- (45) Liu, T.; Yu, L.; Liu, J.; Lu, J.; Bi, X.; Dai, A.; Li, M.; Li, M.; Hu, Z.; Ma, L.; Luo, D.; Zheng, J.; Wu, T.; Ren, Y.; Wen, J.; Pan, F.; Amine, K. Understanding Co Roles towards Developing Co-Free Ni-Rich Cathodes for Rechargeable Batteries. *Nat Energy* 2021, 1–10. <https://doi.org/10.1038/s41560-021-00776-y>.
- (46) Tian, J.; Su, Y.; Wu, F.; Xu, S.; Chen, F.; Chen, R.; Li, Q.; Li, J.; Sun, F.; Chen, S. High-Rate and Cycling-Stable Nickel-Rich Cathode Materials with Enhanced Li + Diffusion Pathway. *Acs Appl Mater Inter* 2015, *8* (1), 582–587. <https://doi.org/10.1021/acsami.5b09641>.
- (47) Heo, K.; Lee, J.-S.; Kim, H.-S.; Kim, J.; Lim, J. Enhanced Electrochemical Performance of Ionic-Conductor Coated  $\text{Li}[\text{Ni}_{0.7}\text{Co}_{0.15}\text{Mn}_{0.15}\text{O}]_2$ . *J Electrochem Soc* 2017, *164* (12), A2398–A2402. <https://doi.org/10.1149/2.0791712jes>.
- (48) Langdon, J.; Manthiram, A. Crossover Effects in Batteries with High-Nickel Cathodes and Lithium-Metal Anodes. *Adv Funct Mater* 2021, 2010267. <https://doi.org/10.1002/adfm.202010267>.
- (49) Andre, D.; Meiler, M.; Steiner, K.; Wimmer, Ch.; Soczka-Guth, T.; Sauer, D. U. Characterization of High-Power Lithium-Ion Batteries by Electrochemical Impedance Spectroscopy. I. Experimental Investigation. *J Power Sources* 2011, *196* (12), 5334–5341. <https://doi.org/10.1016/j.jpowsour.2010.12.102>.
- (50) Gilbert, J. A.; Bareño, J.; Spila, T.; Trask, S. E.; Miller, D. J.; Polzin, B. J.; Jansen, A. N.; Abraham, D. P. Cycling Behavior of NCM523/Graphite Lithium-Ion Cells in the 3–4.4 V Range: Diagnostic Studies of Full Cells and Harvested Electrodes. *J Electrochem Soc* 2016, *164* (1), A6054–A6065. <https://doi.org/10.1149/2.0081701jes>.
- (51) Hou, P.; Zhang, H.; Deng, X.; Xu, X.; Zhang, L. Stabilizing the Electrode/Electrolyte Interface of  $\text{LiNi}_{0.8}\text{Co}_{0.15}\text{Al}_{0.05}\text{O}_2$  through Tailoring Aluminum Distribution in Microspheres as Long-Life, High-Rate, and Safe Cathode for Lithium-Ion Batteries. *Acs Appl Mater Inter* 2017, *9* (35), 29643–29653. <https://doi.org/10.1021/acsami.7b05986>.
- (52) Chen, Y.; Zhao, W.; Zhang, Q.; Yang, G.; Zheng, J.; Tang, W.; Xu, Q.; Lai, C.; Yang, J.; Peng, C. Armoring  $\text{LiNi}_{1/3}\text{Co}_{1/3}\text{Mn}_{1/3}\text{O}_2$  Cathode with Reliable Fluorinated Organic–Inorganic Hybrid Interphase Layer toward Durable High Rate Battery. *Adv Funct Mater* 2020, *30* (19), 2000396. <https://doi.org/10.1002/adfm.202000396>.
- (53) Aurbach, D.; Markovsky, B.; Talyossef, Y.; Salitra, G.; Kim, H.-J.; Choi, S. Studies of Cycling Behavior, Ageing, and Interfacial Reactions of  $\text{LiNi}_{0.5}\text{Mn}_{1.5}\text{O}_4$  and Carbon Electrodes for Lithium-Ion 5-V Cells. *J Power Sources* 2006, *162* (2), 780–789. <https://doi.org/10.1016/j.jpowsour.2005.07.009>.

- (54) Pritzl, D.; Bumberger, A. E.; Wetjen, M.; Landesfeind, J.; Solchenbach, S.; Gasteiger, H. A. Identifying Contact Resistances in High-Voltage Cathodes by Impedance Spectroscopy. *J Electrochem Soc* 2019, *166* (4), A582–A590. <https://doi.org/10.1149/2.0451904jes>.
- (55) Landesfeind, J.; Pritzl, D.; Gasteiger, H. A. An Analysis Protocol for Three-Electrode Li-Ion Battery Impedance Spectra: Part I. Analysis of a High-Voltage Positive Electrode. *J Electrochem Soc* 2017, *164* (7), A1773–A1783. <https://doi.org/10.1149/2.0131709jes>.
- (56) Oswald, S.; Pritzl, D.; Wetjen, M.; Gasteiger, H. A. Novel Method for Monitoring the Electrochemical Capacitance by In Situ Impedance Spectroscopy as Indicator for Particle Cracking of Nickel-Rich NCMs: Part I. Theory and Validation. *J Electrochem Soc* 2020, *167* (10), 100511. <https://doi.org/10.1149/1945-7111/ab9187>.
- (57) Manthiram, A.; Goodenough, J. B. Layered Lithium Cobalt Oxide Cathodes. *Nat Energy* 2021, *6* (3), 323–323. <https://doi.org/10.1038/s41560-020-00764-8>.
- (58) Nishizawa, M.; Yamamura, S. Irreversible Conductivity Change of  $\text{Li}_{1-x}\text{CoO}_2$  on Electrochemical Lithium Insertion/Extraction, Desirable for Battery Applications. *Chem Commun* 1998, *0* (16), 1631–1632. <https://doi.org/10.1039/a802962h>.
- (59) Sim, R.; Lee, S.; Li, W.; Manthiram, A. Influence of Calendering on the Electrochemical Performance of  $\text{LiNi}_{0.9}\text{Mn}_{0.05}\text{Al}_{0.05}\text{O}_2$  Cathodes in Lithium-Ion Cells. *Acs Appl Mater Inter* 2021, *13* (36), 42898–42908. <https://doi.org/10.1021/acsami.1c12543>.
- (60) Weber, R.; Louli, A. J.; Plucknett, K. P.; Dahn, J. R. Resistance Growth in Lithium-Ion Pouch Cells with  $\text{LiNi}_{0.80}\text{Co}_{0.15}\text{Al}_{0.05}\text{O}_2$  Positive Electrodes and Proposed Mechanism for Voltage Dependent Charge-Transfer Resistance. *J Electrochem Soc* 2019, *166* (10), A1779–A1784. <https://doi.org/10.1149/2.0361910jes>.
- (61) Li, Y.; Bettge, M.; Polzin, B.; Zhu, Y.; Balasubramanian, M.; Abraham, D. P. Understanding Long-Term Cycling Performance of  $\text{Li}_{1.2}\text{Ni}_{0.15}\text{Mn}_{0.55}\text{Co}_{0.1}\text{O}_2$  – Graphite Lithium-Ion Cells. *J Electrochem Soc* 2013, *160* (5), A3006–A3019. <https://doi.org/10.1149/2.002305jes>.
- (62) Lin, F.; Markus, I. M.; Nordlund, D.; Weng, T.-C.; Asta, M. D.; Xin, H. L.; Doeff, M. M. Surface Reconstruction and Chemical Evolution of Stoichiometric Layered Cathode Materials for Lithium-Ion Batteries. *Nat Commun* 2014, *5* (1), 3529. <https://doi.org/10.1038/ncomms4529>.
- (63) Li, W.; Liu, X.; Celio, H.; Smith, P.; Dolocan, A.; Chi, M.; Manthiram, A. Mn versus Al in Layered Oxide Cathodes in Lithium-Ion Batteries: A Comprehensive Evaluation on Long-Term Cyclability. *Adv Energy Mater* 2018, *8* (15), 1703154. <https://doi.org/10.1002/aenm.201703154>.
- (64) Zhang, X.; Zou, L.; Xu, Y.; Cao, X.; Engelhard, M. H.; Matthews, B. E.; Zhong, L.; Wu, H.; Jia, H.; Ren, X.; Gao, P.; Chen, Z.; Qin, Y.; Kompella, C.; Arey, B. W.; Li, J.; Wang, D.; Wang, C.; Zhang, J.; Xu, W. Advanced Electrolytes for Fast-Charging High-Voltage Lithium-Ion

Batteries in Wide-Temperature Range. *Adv Energy Mater* 2020, 10 (22), 2000368.  
<https://doi.org/10.1002/aenm.202000368>.

(65) Xie, Q.; Li, W.; Dolocan, A.; Manthiram, A. Insights into Boron-Based Polyanion-Tuned High-Nickel Cathodes for High-Energy-Density Lithium-Ion Batteries. *Chem Mater* 2019, 31 (21), 8886–8897. <https://doi.org/10.1021/acs.chemmater.9b02916>.

(66) Liu, S.; Wang, L.; Zhang, C.; Chu, B.; Wang, C.; Huang, T.; Yu, A. Dynamic Evolution of Cathode–Electrolyte Interface of LiNi<sub>0.6</sub>Co<sub>0.2</sub>Mn<sub>0.2</sub>O<sub>2</sub> during the Initial Charge–Discharge Process. *J Power Sources* 2019, 438, 226979. <https://doi.org/10.1016/j.jpowsour.2019.226979>.

(67) Li, J.; Manthiram, A. A Comprehensive Analysis of the Interphasial and Structural Evolution over Long-Term Cycling of Ultrahigh-Nickel Cathodes in Lithium-Ion Batteries. *Adv Energy Mater* 2019, 9 (45), 1902731. <https://doi.org/10.1002/aenm.201902731>.

(68) Edström, K.; Gustafsson, T.; Thomas, J. O. The Cathode–Electrolyte Interface in the Li-Ion Battery. *Electrochim Acta* 2004, 50 (2–3), 397–403.  
<https://doi.org/10.1016/j.electacta.2004.03.049>.

(69) Verma, P.; Maire, P.; Novák, P. A Review of the Features and Analyses of the Solid Electrolyte Interphase in Li-Ion Batteries. *Electrochim Acta* 2010, 55 (22), 6332–6341.  
<https://doi.org/10.1016/j.electacta.2010.05.072>.

(70) Vissers, D. R.; Chen, Z.; Shao, Y.; Engelhard, M.; Das, U.; Redfern, P.; Curtiss, L. A.; Pan, B.; Liu, J.; Amine, K. Role of Manganese Deposition on Graphite in the Capacity Fading of Lithium Ion Batteries. *Acs Appl Mater Inter* 2016, 8 (22), 14244–14251.  
<https://doi.org/10.1021/acsami.6b02061>.

(71) Betz, J.; Brinkmann, J.; Nölle, R.; Lürenbaum, C.; Kolek, M.; Stan, M. C.; Winter, M.; Placke, T. Cross Talk between Transition Metal Cathode and Li Metal Anode: Unraveling Its Influence on the Deposition/Dissolution Behavior and Morphology of Lithium. *Adv Energy Mater* 2019, 9 (21), 1900574. <https://doi.org/10.1002/aenm.201900574>.

(72) Cui, Z.; Xie, Q.; Manthiram, A. Zinc-Doped High-Nickel, Low-Cobalt Layered Oxide Cathodes for High-Energy-Density Lithium-Ion Batteries. *Acs Appl Mater Inter* 2021, 13 (13), 15324–15332. <https://doi.org/10.1021/acsami.1c01824>.

(73) Pritzl, D.; Landesfeind, J.; Solchenbach, S.; Gasteiger, H. A. An Analysis Protocol for Three-Electrode Li-Ion Battery Impedance Spectra: Part II. Analysis of a Graphite Anode Cycled vs. LNMO. *J Electrochem Soc* 2018, 165 (10), A2145–A2153.  
<https://doi.org/10.1149/2.0461810jes>.




(74) Li, W.; Kim, U.-H.; Dolocan, A.; Sun, Y.-K.; Manthiram, A. Formation and Inhibition of Metallic Lithium Microstructures in Lithium Batteries Driven by Chemical Crossover. *Acs Nano* 2017, 11 (6), 5853–5863. <https://doi.org/10.1021/acsnano.7b01494>.

- (75) Klein, S.; Harte, P.; Henschel, J.; Bärmann, P.; Borzutzki, K.; Beuse, T.; Wickeren, S.; Heidrich, B.; Kasnatscheew, J.; Nowak, S.; Winter, M.; Placke, T. On the Beneficial Impact of Li<sub>2</sub>CO<sub>3</sub> as Electrolyte Additive in NCM523 || Graphite Lithium Ion Cells Under High-Voltage Conditions. *Adv Energy Mater* 2021, 2003756. <https://doi.org/10.1002/aenm.202003756>.
- (76) Klein, S.; Wickeren, S. van; Röser, S.; Bärmann, P.; Borzutzki, K.; Heidrich, B.; Börner, M.; Winter, M.; Placke, T.; Kasnatscheew, J. Understanding the Outstanding High-Voltage Performance of NCM523||Graphite Lithium Ion Cells after Elimination of Ethylene Carbonate Solvent from Conventional Electrolyte. *Adv Energy Mater* 2021, 2003738. <https://doi.org/10.1002/aenm.202003738>.
- (77) Li, J.; Liu, H.; Xia, J.; Cameron, A. R.; Nie, M.; Botton, G. A.; Dahn, J. R. The Impact of Electrolyte Additives and Upper Cut-off Voltage on the Formation of a Rocksalt Surface Layer in LiNi<sub>0.8</sub>Mn<sub>0.1</sub>Co<sub>0.1</sub>O<sub>2</sub> Electrodes. *J Electrochem Soc* 2017, 164 (4), A655–A665. <https://doi.org/10.1149/2.0651704jes>.
- (78) Kim, Y.; Park, H.; Shin, K.; Henkelman, G.; Warner, J. H.; Manthiram, A. Rational Design of Coating Ions via Advantageous Surface Reconstruction in High-Nickel Layered Oxide Cathodes for Lithium-Ion Batteries. *Adv Energy Mater* 2021, 2101112. <https://doi.org/10.1002/aenm.202101112>.
- (79) Jo, E.; Park, J.-H.; Park, J.; Hwang, J.; Chung, K. Y.; Nam, K.-W.; Kim, S. M.; Chang, W. Different Thermal Degradation Mechanisms: Role of Aluminum in Ni-Rich Layered Cathode Materials. *Nano Energy* 2020, 78, 105367. <https://doi.org/10.1016/j.nanoen.2020.105367>.
- (80) Jo, E.; Hwang, S.; Kim, S. M.; Chang, W. Investigating the Kinetic Effect on Structural Evolution of Li<sub>x</sub>Ni<sub>0.8</sub>Co<sub>0.15</sub>Al<sub>0.05</sub>O<sub>2</sub> Cathode Materials during the Initial Charge/Discharge. *Chem Mater* 2017, 29 (7), 2708–2716. <https://doi.org/10.1021/acs.chemmater.6b03282>.
- (81) Xu, K. Nonaqueous Liquid Electrolytes for Lithium-Based Rechargeable Batteries. *Chem Rev* 2004, 104 (10), 4303–4418. <https://doi.org/10.1021/cr030203g>.
- (82) Wu, Y.; Liu, X.; Wang, L.; Feng, X.; Ren, D.; Li, Y.; Rui, X.; Wang, Y.; Han, X.; Xu, G.-L.; Wang, H.; Lu, L.; He, X.; Amine, K.; Ouyang, M. Development of Cathode-Electrolyte-Interphase for Safer Lithium Batteries. *Energy Storage Mater* 2021, 37, 77–86. <https://doi.org/10.1016/j.ensm.2021.02.001>.
- (83) Liu, X.; Ren, D.; Hsu, H.; Feng, X.; Xu, G.-L.; Zhuang, M.; Gao, H.; Lu, L.; Han, X.; Chu, Z.; Li, J.; He, X.; Amine, K.; Ouyang, M. Thermal Runaway of Lithium-Ion Batteries without Internal Short Circuit. *Joule* 2018, 2 (10), 2047–2064. <https://doi.org/10.1016/j.joule.2018.06.015>.
- (84) Myung, S.-T.; Lee, K.-S.; Yoon, C. S.; Sun, Y.-K.; Amine, K.; Yashiro, H. Effect of AlF<sub>3</sub> Coating on Thermal Behavior of Chemically Delithiated Li<sub>0.35</sub>[Ni<sub>1/3</sub>Co<sub>1/3</sub>Mn<sub>1/3</sub>]O<sub>2</sub>. *J Phys Chem C* 2010, 114 (10), 4710–4718. <https://doi.org/10.1021/jp9082322>.

(85) MacNeil, D. D.; Dahn, J. R. The Reactions of  $\text{Li}_{0.5}\text{CoO}_2$  with Nonaqueous Solvents at Elevated Temperatures. *J Electrochem Soc* 2002, *149* (7), A912–A919. <https://doi.org/10.1149/1.1483865>.

(86) Cormier, M. M. E.; Zhang, N.; Liu, A.; Li, H.; Inglis, J.; Dahn, J. R. Impact of Dopants (Al, Mg, Mn, Co) on the Reactivity of  $\text{Li}_x\text{NiO}_2$  with the Electrolyte of Li-Ion Batteries. *J Electrochem Soc* 2019, *166* (13), A2826–A2833. <https://doi.org/10.1149/2.0491913jes>.

## For Table of Contents Only

Cycling performance	✗	✓	✓
Reduced transition metal crossover	✗	✗	✓
Thermal stability	✗	✗	✓
	 F-rich CEI NM	 O-rich CEI NMC	 C-rich CEI NMA